

\mathbb{Z}_2 Vortex Crystal Candidate in the Triangular $S = 1/2$ Quantum Antiferromagnet

J. Nagl,^{1,*} K. Yu. Povarov,² B. Duncan,¹ C. Näppi,¹ D. Khalyavin,³ P. Manuel,³
 F. Orlandi,³ J. Sourd,² B. V. Schwarze,² F. Husstedt,² S. A. Zvyagin,² O. Zaharko,⁴
 P. Steffens,⁵ A. Hiess,^{5,6} D. Allan,⁷ S. Barnett,⁷ Z. Yan,¹ S. Gvasaliya,¹ and A. Zheludev^{1,†}

¹Laboratory for Solid State Physics, ETH Zürich, 8093 Zürich, Switzerland

²Dresden High Magnetic Field Laboratory (HLD-EMFL) and Würzburg-Dresden Cluster of Excellence ct.qmat, Helmholtz-Zentrum Dresden-Rossendorf (HZDR), 01328 Dresden, Germany

³ISIS Facility, Rutherford Appleton Laboratory, Chilton, Didcot, Oxon OX11 0QX, United Kingdom

⁴PSI Center for Neutron and Muon Sciences, Forschungsstrasse 111, 5232 Villigen, PSI, Switzerland

⁵Institut Laue-Langevin, 71 avenue des Martyrs, CS 20156, 38042 Grenoble Cedex 9, France

⁶European Spallation Source ERIC, P.O. Box 176, 22100 Lund, Sweden

⁷Diamond Light Source, Harwell Science and Innovation Campus, Didcot, Oxfordshire OX11 0DE, UK
 (Dated: December 2, 2025)

The prospect of merging the paradigms of geometric frustration on a triangular lattice and bond anisotropies in the strong spin-orbit coupling limit holds tremendous promise in the ongoing hunt for exotic quantum materials. Here we identify a new candidate system to realize such physics, the organic quantum antiferromagnet $(\text{CD}_3\text{ND}_3)_2\text{NaRuCl}_6$. We report a combination of thermodynamic, magneto-elastic and neutron scattering experiments on single-crystals to determine the phase diagram in axial magnetic fields $\mathbf{H} \parallel \mathbf{c}$ and propose a minimal model Hamiltonian. $(\text{CD}_3\text{ND}_3)_2\text{NaRuCl}_6$ displays an ideal triangular arrangement of Ru^{3+} ions adopting the spin-orbital entangled $j_{\text{eff}} = 1/2$ state. It hosts residual magnetic order below $T_N = 0.23$ K and a highly unusual $H - T$ phase diagram including three different incommensurate states. Spin-waves in the high-field polarized regime are well described by a Heisenberg-like triangular lattice Hamiltonian with a potential sub-leading bond dependent anisotropy term. We discuss possible candidate magnetic structures in the various observed phases and propose two mechanisms that could explain the field-dependent incommensurability, requiring either a small ferromagnetic Kitaev term or a tiny magneto-elastic $J - J'$ isosceles distortion driven by pseudospin-lattice coupling. We argue that the multi- \mathbf{q} ground state in zero magnetic field is a prime candidate for hosting the \mathbb{Z}_2 vortex crystal proposed on the triangular Heisenberg-Kitaev model. $(\text{CD}_3\text{ND}_3)_2\text{NaRuCl}_6$ is the first member in an extended family of quantum triangular lattice magnets, providing a new playground to study the interplay of geometric frustration and spin-orbit effects.

Quantum antiferromagnets on a $S = 1/2$ frustrated triangular lattice pose one of the oldest and most influential paradigms in quantum magnetism [1–3]. Even the basic Heisenberg model continues to draw considerable interest, as good material prototypes have only recently become available, finally allowing for concrete comparison to theoretical predictions of exchange renormalization and magnon decay [4–6]. Away from the isotropic limit, the possibility of a quantum spin liquid ground state remains an intensely debated issue [7, 8], with numerous theoretical predictions and only a handful of promising material candidates. Recent experimental work has focused mostly on Co^{2+} [5, 9, 10] and Yb^{3+} [6, 11, 12] systems, with the heavy $4d$ and $5d$ transition metals going largely unexplored despite their prominence in the context of bond dependent interactions in Kitaev-honeycomb systems [13, 14]. Thus, combining such bond anisotropies with a frustrated lattice topology poses a promising route to realizing new emergent quantum phases.

One such class of exotic ground states - often stabilized by anisotropy and exchange competition - are the

topological spin textures [15]. The triangular Heisenberg antiferromagnet has long been known to host \mathbb{Z}_2 vortices as topological excitations [16], particle-like “twists” in the familiar 120° three-sublattice order. Recently it was realized that they become thermodynamically stable when Kitaev interactions are invoked [17]. Indeed, even a tiny Kitaev term $|K|/J \ll 1$ is enough to condense them into the ground state, forming an incommensurate (IC) triangular superlattice of \mathbb{Z}_2 vortices. This is analogous to the formation of skyrmions in chiral helimagnets [18–21] or Abrikosov vortices in type-II superconductors [22–24]. These predictions have garnered intense theoretical interest [25–33], in part because this phase appears to be quite robust in the Heisenberg-Kitaev model and may not require excessive fine-tuning of interactions as in the elusive spin-liquids [8]. An experimental implementation of the \mathbb{Z}_2 vortex crystal currently remains open: Only a scant few $4d/5d$ compounds have been proposed to realize the parent Hamiltonian [25, 26, 34] and none are available in single crystalline form, keeping studies in their infancy.

We address this problem by identifying an entirely new candidate material to host such physics, namely the recently discovered organic quantum antiferromagnetic insulator $(\text{CD}_3\text{ND}_3)_2\text{NaRuCl}_6$ [35], crystallizing in a trigonal $P\bar{3}m1$ structure (Fig. 1a). Its magnetism

* jnagl@ethz.ch

† zhelud@ethz.ch; <http://www.neutron.ethz.ch/>

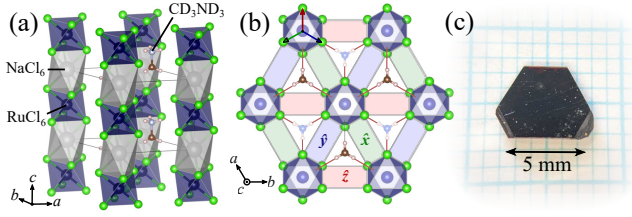


FIG. 1. Crystal structure of $(\text{CD}_3\text{ND}_3)_2\text{NaRuCl}_6$. (a) Schematic view of the chemical structure, with AA-stacked triangular planes of Ru^{3+} ions. (b) Top-down view of the triangular lattice, emphasizing the three different bond types with parallel-edge RuCl_6 octahedra. (c) A typical single-crystal sample of $(\text{CD}_3\text{ND}_3)_2\text{NaRuCl}_6$.

originates from the low-spin $4d^5$ Ru^{3+} ions with nearly perfect octahedral coordination, leaving an unquenched $l = 1$ orbital moment that should engender spin-orbital entangled $j_{\text{eff}} = 1/2$ degrees of freedom at low temperatures. The material realizes an AA-stacked triangular lattice of RuCl_6 octahedra in the crystallographic ab plane (Fig. 1b), with comparable *in*-plane and *inter*-plane distances $a = 7.14$ Å and $c = 6.74$ Å. As shown in the supplement [36], it undergoes a subtle structural transition to $P\bar{3}$ at $T^* \simeq 118$ K. However, the ideal triangular coordination of Ru is preserved and Dzyaloshinskii-Moriya terms remain forbidden by symmetry down to the lowest temperatures. The bonds connecting RuCl_6 octahedra are not of edge-sharing type as in the famous Kitaev-type honeycomb materials [13]. Instead they display a parallel-edge geometry, nevertheless with two interfering superexchange pathways and three orthogonal bond types (Fig. 1b). A significant Kitaev-term has been proposed for such configurations by several authors [14, 25, 26], but these claims have yet to be verified experimentally due to a lack of material candidates available in single crystalline form.

In this work, we present a thorough investigation of the magnetic ground states and excitations on single crystals of $(\text{CD}_3\text{ND}_3)_2\text{NaRuCl}_6$ through a combination of neutron scattering and bulk thermodynamic probes. We show that the pseudospin wavefunctions are indeed dominated by the ideal $j_{\text{eff}} = 1/2$ state. Below $T_{\text{N}1} \approx 0.23$ K, $(\text{CD}_3\text{ND}_3)_2\text{NaRuCl}_6$ exhibits a two-step transition into a long-range ordered ground state. The latter turns out to be a complex multi- \mathbf{q} order with sets of three IC Bragg peaks around the K and H-points, making it a strong contender for the \mathbb{Z}_2 vortex crystal phase - with the additional complication of weak AFM inter-plane interactions. In an axial magnetic field $\mathbf{H} \parallel \mathbf{c}$, we observe a cascade of *seven* field-induced ordered phases with several commensurate-incommensurate transitions. While the commensurate states in the center of the phase diagram may be understood through order-by-disorder selection on a semi-classical Heisenberg model, the three IC phases towards low/high fields point to the relevance of anisotropies. The spin-wave dispersion in the field-polarized regime is captured by a quasi-2D nearest neighbor

Heisenberg triangular lattice model with a potential sub-leading bond dependent term. $(\text{CD}_3\text{ND}_3)_2\text{NaRuCl}_6$ is the first member in an entirely new family of quantum triangular lattice magnets based on heavy $4d/5d$ transition metals, providing fertile grounds to explore the incommensurate/topological phases emerging from the interplay between geometric frustration and spin-orbit coupling.

I. RESULTS

A. Basic Properties & Single-Ion Physics

In Fig. 2(b) we present the uniform magnetic susceptibility of $(\text{CD}_3\text{ND}_3)_2\text{NaRuCl}_6$ along the principal crystallographic axes. For $\mathbf{H} \parallel \mathbf{c}$ we observe a linear Curie-Weiss behavior up to room temperature in the inverse susceptibility, whereas for in-plane fields, $\chi_{ab}^{-1}(T)$ exhibits a strong non-linear bending, indicative of crystal-field effects. The data exhibit a pronounced easy-axis anisotropy, reaching $\chi_c/\chi_{ab} \sim 2.3$ in the low-temperature limit. A simple Curie-Weiss analysis in the range 10 – 40 K results in an average Weiss temperature of $\theta_{\text{CW}} \approx -3.8$ K (see Table I for details), indicative of moderate antiferromagnetic interactions. The single-ion anisotropy is also reflected in the effective moments $\mu_{\text{eff}} = g\sqrt{S(S+1)}\mu_B$. These point to anisotropic $S_{\text{eff}} = 1/2$ degrees of freedom with $g_c/g_{ab} \sim 1.6$, typical for systems with an unquenched orbital contribution. Magnetometry data on the same sample [see Fig. 2(c)] begin to show significant deviations from a non-interacting Brillouin function below $\lesssim 10$ K, consistent with an onset of short-range spin correlations.

More precise g -factor values are obtained from electron spin resonance (ESR) measurements. For both longitudinal and transverse field geometries, we observe a single resonance line at $T = 1.5$ K, as illustrated in Fig. 3 - a rare example of resonance in a strongly correlated system of Ru^{3+} magnetic ions [37]. The frequency-field dependence is linear, suggesting simple Larmor precession at these temperatures. Fits to $h\nu = g\mu_B\mu_0 H$ yield $g_{ab} = 1.53(1)$ and $g_c = 2.69(1)$, nicely matching our estimates from susceptibility. We detect no apparent change in g -factors with temperature [36].

For Ru^{3+} transition metal ions with $4d^5$ electronic configuration, the octahedral crystal field results in a single hole residing in the t_{2g} manifold, forming a spin $S = 1/2$ and an effective orbital moment $l_{\text{eff}} = 1$. These

TABLE I. Fit results for a Curie-Weiss analysis in the temperature range $10 \text{ K} \leq T \leq 40 \text{ K}$.

	θ_{CW} (K)	μ_{eff} (μ_B)	g
$\mathbf{H} \parallel a$	-3.82	1.42	1.64
$\mathbf{H} \parallel c$	-3.93	2.32	2.68

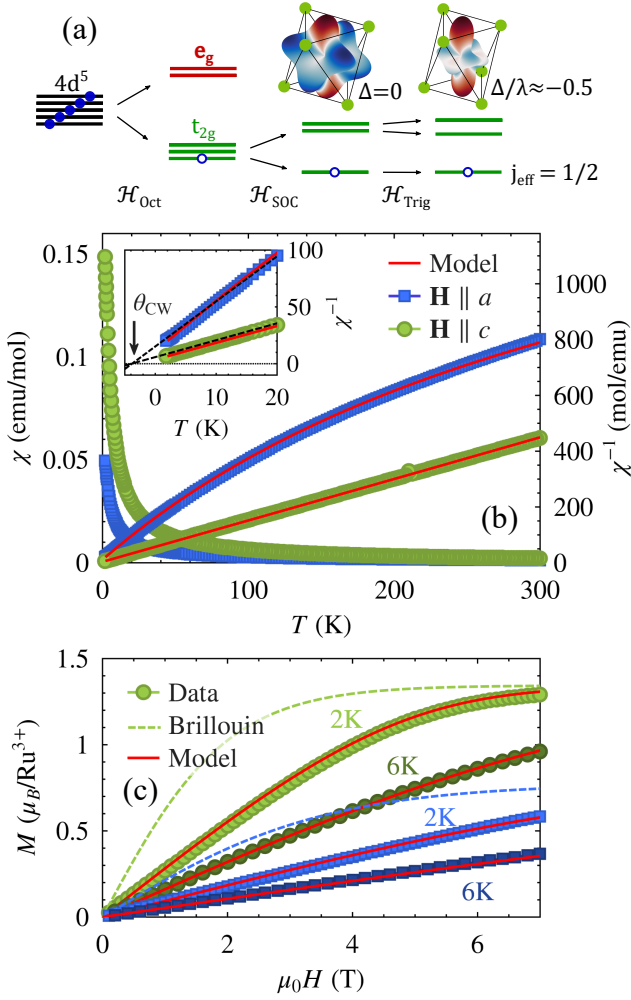


FIG. 2. Single-ion physics and mean-field correlations in $(\text{CD}_3\text{ND}_3)_2\text{NaRuCl}_6$. (a) Schematic of the energy spectrum for a single Ru^{3+} ion. The free-ion multiplet is split by the cubic crystal electric field, the spin-orbit coupling λ and a trigonal distortion Δ . An inset visualizes the spatial shape of the pseudospin wavefunctions, both for the ideal cubic case ($\Delta = 0$) and for the parameters $\Delta/\lambda \approx -0.5$ relevant to $(\text{CD}_3\text{ND}_3)_2\text{NaRuCl}_6$. Red/blue color indicates spin up/down of the hole, mixed together in the spin-orbital entangled $j_{\text{eff}} = 1/2$ ground state. (b) Magnetic susceptibility for a small probing field $\mu_0 H = 0.1$ T along the principal crystallographic axes. The inset shows a low-temperature Curie-Weiss fit. (c) Magnetization curves at various temperatures (markers), along with Brillouin function expected in absence of two-ion correlations (dashed lines). Red lines in (b,c) represent the calculated magnetic response based on the single-ion + mean-field model discussed in the text.

states are further split by the strong spin-orbit coupling $\lambda \sim 0.15$ eV [38] and by a potential trigonal distortion Δ . This is borne out in the following local single-ion Hamiltonian

$$\mathcal{H} = \lambda \hat{\ell} \cdot \hat{\mathbf{S}} + \Delta \hat{\ell}_z^2 - \mu_B \mathbf{H} \cdot \hat{\mathbf{M}} \quad (1)$$

where $\hat{\mathbf{M}} = 2\hat{\mathbf{S}} - k\hat{\ell}$ is the on-site magnetization of the hole and $k \lesssim 1$ accounts for a small reduction in orbital

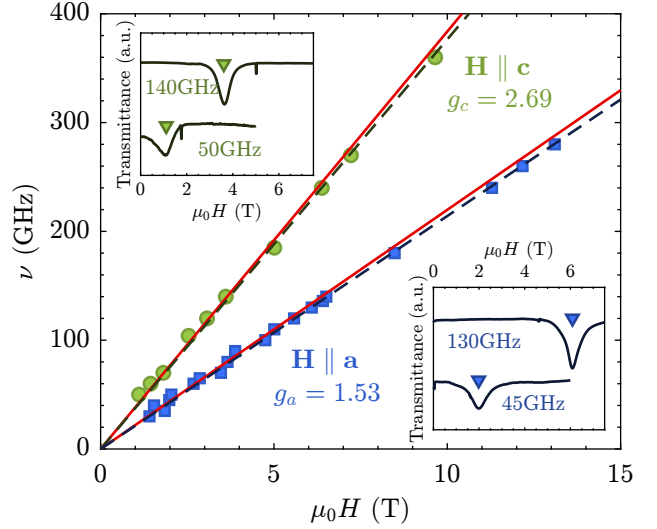


FIG. 3. Frequency-field diagram of ESR excitations measured at $T = 1.5$ K for both $\mathbf{H} \parallel \mathbf{c}$ (green) and $\mathbf{H} \parallel \mathbf{a}$ (blue) field orientations. Dashed lines represent linear fits to the function $h\nu = g\mu_B\mu_0 H$, while solid red lines show calculations based on the single-ion + mean-field model discussed in the text. ESR spectra at selected frequencies are presented as insets. Characteristic dips in transmittance correspond to the Larmor resonant field at given frequency, while sharp features are caused by the $g = 2.00$ DPPH marker.

moment due to anion hybridization [39]. In the cubic limit $|\Delta/\lambda| \ll 1$, the ground state is a spin-orbital entangled $j_{\text{eff}} = 1/2$ Kramers doublet with equal weights on all three t_{2g} orbitals [40].

The Hamiltonian parameters can be extracted from a global fit to the susceptibility, magnetization and ESR data. In order to account for incipient two-ion correlations, we introduce a Weiss molecular field $\mathbf{H} \rightarrow \mathbf{H}_{\text{ext}} + \mathbf{H}_{\text{MF}}$ and solve the resulting eigenvalue problem self-consistently. We obtain $\lambda = 153.3$ meV, $\Delta = -77.9$ meV and $J_{\text{MF}} = 1.71$ K [36], where the latter is a mean-field exchange parameter setting the strength of the molecular field. Our fit results are shown in Fig. 2 as red lines, confirming excellent agreement among different probes. With $\Delta/\lambda \simeq -0.51$, we are still within the spin-orbital entangled regime. The ground state wavefunctions remain dominated by the ideal $j_{\text{eff}} = 1/2$ state, though the magnetization density acquires a notable easy-axis character through the trigonal distortion, with slightly more weight on the $\ell_z = \pm 1$ states (see Fig. 2(a) and [36]). The data are well described by a mean-field exchange constant J_{MF} of Heisenberg type - which would correspond to $\theta_{\text{CW}} \approx -2.6$ K - with no signs of XXZ anisotropy within estimated standard deviations. Given the above trigonal distortion, we expect the dominant superexchange scale to be of Heisenberg type [41], with potential bond anisotropies only taking a sub-leading role. But as we discuss below, even a small bond-dependent term can induce qualitatively new physics on the triangular lattice [17, 25].

B. Calorimetry

In Fig. 4(a) we show the temperature dependence of the specific heat capacity in $(\text{CD}_3\text{ND}_3)_2\text{NaRuCl}_6$ (note the logarithmic scale). We focus on the low-temperature regime $T \lesssim 4$ K, where the lattice is frozen and only magnetic degrees of freedom remain. There is a broad upturn in $C_p(T)$ around θ_{CW} , which we associate with the onset of short-range magnetic correlations. It develops into a plateau between 1 K and 0.2 K, followed by a sharp anomaly indicative of a phase transition to magnetic long-range order. The latter takes place in two steps: Zooming in close to the critical region reveals both a shoulder feature at $T_{\text{N1}} = 0.23$ K and a sharp peak at $T_{\text{N2}} = 0.215$ K. In the ordered phase, the heat capacity fits either to a (gapless) power-law $C_p \propto T^x$ with $x \approx 4.5$, or to an activated behavior $C_p \propto e^{-\Delta/T}$ with $\Delta \approx 0.5$ K. While such a strong power-law seems rather unlikely to capture the physics at hand, a small excitation gap ~ 0.5 K would be consistent with the magnetic energy scale, perhaps pointing to some anisotropies that break the $O(3)$ symmetry in spin-space. The change in magnetic entropy $\Delta S = \int C_p/T$ [see Fig. 4(b)] is extracted through numerical integration of the heat capacity data. It reaches a plateau around 4 K, nicely extrapolating to $R \ln(2)$ as expected for $j_{\text{eff}} = 1/2$ degrees of freedom.

In an axial magnetic field $\mathbf{H} \parallel \mathbf{c}$, the two transitions at T_{N1} and T_{N2} begin to separate [see temperature scans in Fig. 5(a)]. Magnetic order is enhanced by small applied fields, creating a reentrant bulge in the phase diagram with a maximal ordering temperature $T_{\text{N1}}^{\text{max}} \approx 0.3$ K. Meanwhile, T_{N2} moves towards lower temperatures and becomes suppressed, disappearing completely around 1.3 T. A small anomaly re-emerges above 1.6 T and seems to meet the main transition line at a bicritical point near $\mu_0 H_{\text{bc}} \approx 2.2$ T. At higher fields, we observe an additional pre-saturation phase, evident in field scans such as Fig. 5(c) as two consecutive anomalies around 2.65 and 2.95 T. Finally, above 3.2 T we enter the pseudospin polarized regime where specific heat becomes gapped. We summarize this in the preliminary phase diagram shown in Fig. 5(b), reminiscent of the 2D Heisenberg TLAF [42–44] except for the extra pre-saturation phase. The spin gap increases linearly with field [white squares, denoting the Schottky maximum positions in $C_p(T, H)$]. A fit to $T_{\text{max}} \propto (H - H_{\text{sat}})^{z\nu}$ yields a saturation field $H_{\text{sat}} = 3.20(2)$ T and crossover exponent $z\nu = 1.15(5)$ for the proximate quantum critical point.

C. Magnetoelastic Effects

Given the spin-orbital entangled ground state doublet, the onset of magnetic order may have significant effects on the lattice (and vice versa). To probe such magneto-elastic coupling, we employ a combination of

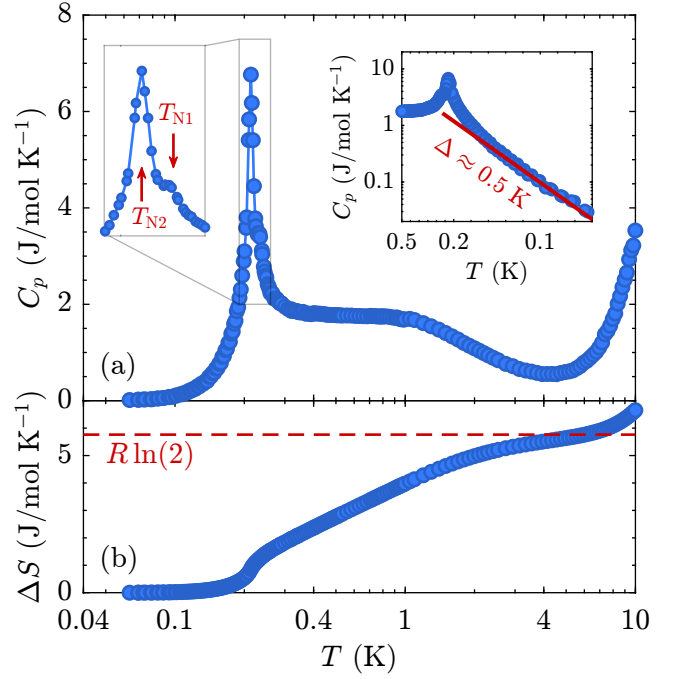


FIG. 4. Temperature dependence of specific heat in $(\text{CD}_3\text{ND}_3)_2\text{NaRuCl}_6$. (a) Measured heat capacity $C_p(T)$ in zero magnetic field, exhibiting a two-step transition to magnetic long-range order. Left inset: Zoom-in on the critical region, showing two separate anomalies at T_{N1} and T_{N2} K. Right inset: Arrhenius plot depicting the activated behavior in the ordered state. (b) Entropy change $\Delta S(T)$ obtained through numerical integration of the specific heat.

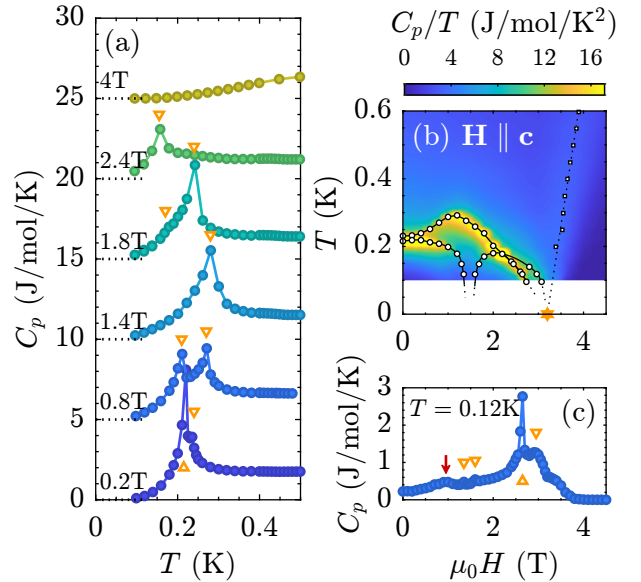


FIG. 5. Specific heat of $(\text{CD}_3\text{ND}_3)_2\text{NaRuCl}_6$ in axial magnetic fields $\mathbf{H} \parallel \mathbf{c}$. (a) Exemplary $C_p(T)$ scans for various fixed fields H . (b) Preliminary phase diagram. Color shows C_p/T data, while circles identify sharp anomalies in heat capacity and squares denote the Schottky maximum above H_{sat} . (c) Exemplary $C_p(H)$ scan at $T = 0.12$ K. Orange triangles highlight the peak positions in the data. Red arrow marks a broad maximum in C_p discussed in the text.

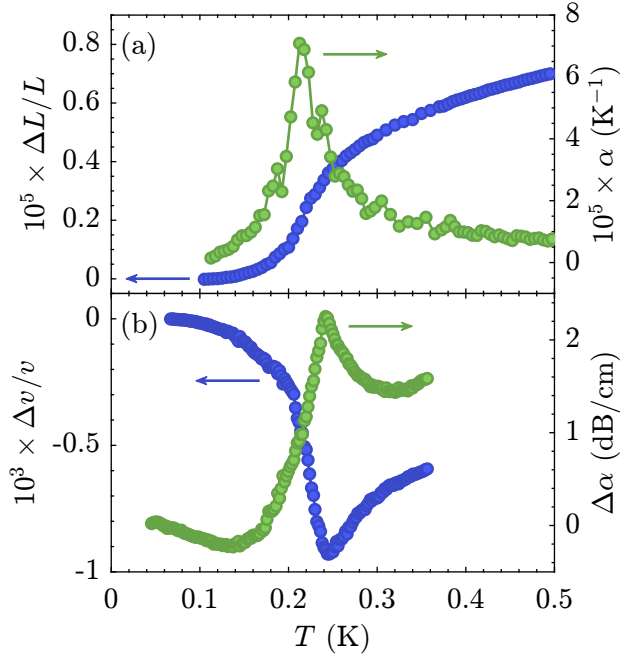


FIG. 6. Magnetoelastic effects in $(\text{CD}_3\text{ND}_3)_2\text{NaRuCl}_6$. (a) Temperature dependent sample dilation $\Delta l/l$ along the \mathbf{a}^* -axis, along with its numerical derivative, the thermal expansion coefficient $\alpha = \frac{1}{l} \frac{\partial \Delta l}{\partial T}$. (b) Relative changes in sound velocity and attenuation for the longitudinal c_{11} -mode.

dilatometry and ultrasound measurements. In Fig. 6(a) we show the relative change in sample length $\Delta l/l$ along \mathbf{a}^* against temperature. The lattice contracts significantly below T_N , which may be understood through an exchange-striction mechanism [36, 45]: Exchange interactions depend on inter-atomic distances, so each bond acquires an extra stiffness contribution $\propto \langle \hat{\mathbf{S}}_i \cdot \hat{\mathbf{S}}_j \rangle$ in the ordered state and the crystal shrinks to minimize the free energy. Particularly interesting is the numerical derivative of this length change, i.e. the thermal expansion coefficient $\alpha(T) = \frac{1}{l} \frac{\partial \Delta l}{\partial T}$. Through Ehrenfest relations, the discontinuity in thermal expansion and heat capacity at T_N can be combined to estimate the initial pressure dependence of the transition temperature $\partial T_N / \partial p = V_m T_N \frac{\Delta \alpha_{\text{crit}}}{\Delta C_p^{\text{crit}}}$ where V_m is the molar volume. We obtain a *huge* uniaxial pressure dependence $\partial \ln(T_N) / \partial p_{100} \approx 250\%$, indicating that the magnetic structure is highly sensitive to in-plane strains. Analogous thermal expansion effects along the \mathbf{c} -axis are an order of magnitude weaker [36], consistent with a quasi-2D hierarchy of superexchange interactions.

Complementary information can be gleaned from ultrasound, where we measure relative changes in sound velocity $\Delta v/v$ and attenuation $\Delta\alpha$ through the transition [see Fig. 6(b)]. We focus on the longitudinal c_{11} -mode, propagating in the triangular plane with a sound velocity $v_{11} \simeq 2.1$ km/s. Both probes exhibit strong anomalies at T_N : Whereas the phonon frequencies soften near the onset of magnetic correlations (similar to Kohn

anomaly), the attenuation - like all transport coefficients [46] - diverges at the transition, as sound waves become damped by critical fluctuations. Assuming an exchange-striction framework, we can estimate the magnetoelastic coupling constant $g_\Gamma \equiv \frac{\partial J}{\partial \varepsilon_\Gamma}$ for a particular strain component ε_Γ . For the A_1 “breathing” distortion of the triangular plane that we probe experimentally, we obtain $g_{A1} \sim 40$ K [36]. This is an order of magnitude larger than in similar triangular lattice systems like $\text{Ba}_3\text{CoSb}_2\text{O}_9$ [47] or Cs_2CuCl_4 [48, 49], signaling a strong coupling between pseudospin and lattice degrees of freedom.

This is borne out in additional field-induced measurements summarized in Fig. 7, revealing a much richer phase evolution than anticipated from heat capacity. The most pronounced anomalies appear in the region between 0.9 T and 1.6 T, where the sample length exhibits a plateau-like feature, while the sound velocity and attenuation show clear dips and peaks, respectively. The first of these features neatly matches a broad maximum observed in $C_p(H)$ around 0.9 T [red arrow in Fig. 5(c)]. Further anomalies become visible especially in the magnetostriction coefficient $\lambda(H) = \frac{1}{\mu_0 l} \frac{\partial \Delta l}{\partial H}$ [Fig. 7(d)] or the analogous numerical derivatives of $\Delta v/v$ and $\Delta\alpha$, revealing a cascade of field-induced phase transitions. In the low-temperature limit, there are six phases clearly identified by several probes, with transition fields near 0.9, 1.35, 1.6, 2.1, 2.6 and 3.2 T. With increasing temperature, all features gradually become broadened and disappear, leaving behind only paramagnetic behavior above $T_N^{\text{max}} \approx 0.3$ K.

By combining the anomalies from all probes described above, we obtain the $H - T$ phase diagram depicted in Fig. 8(a). Note the presence of another slim presaturation phase between 2.6 and 2.9 T, stable only below $T \sim 80$ mK. The latter is clearly identified only by neutron diffraction (see below), though our ultrasound data do show some subtle features in this regime.

D. Magnetization Plateau

While the sequence of phases in Fig. 8(a) looks relatively complicated, there is an obvious starting point for understanding the magnetic behavior: The third phase, labeled “ $\uparrow\uparrow\downarrow$ ”. Its reentrant shape in the center of the $H - T$ phase diagram and the second order transition line directly into the paramagnetic state are both typical features of the $m = 1/3$ magnetization plateau expected to emerge in an ideal Heisenberg triangular lattice system [42–44]. Being a collinear state, it is most strongly preferred by order-by-disorder and is therefore relatively stable with respect to most Hamiltonian perturbations. To confirm this, we carried out magnetization measurements at $T = 100$ mK using a home-made Faraday balance setup [50], shown in Fig. 8(b). Indeed, between 1.3 T and 1.55 T we observe a weak but distinctive kink in the magnetization curve, which is otherwise mostly

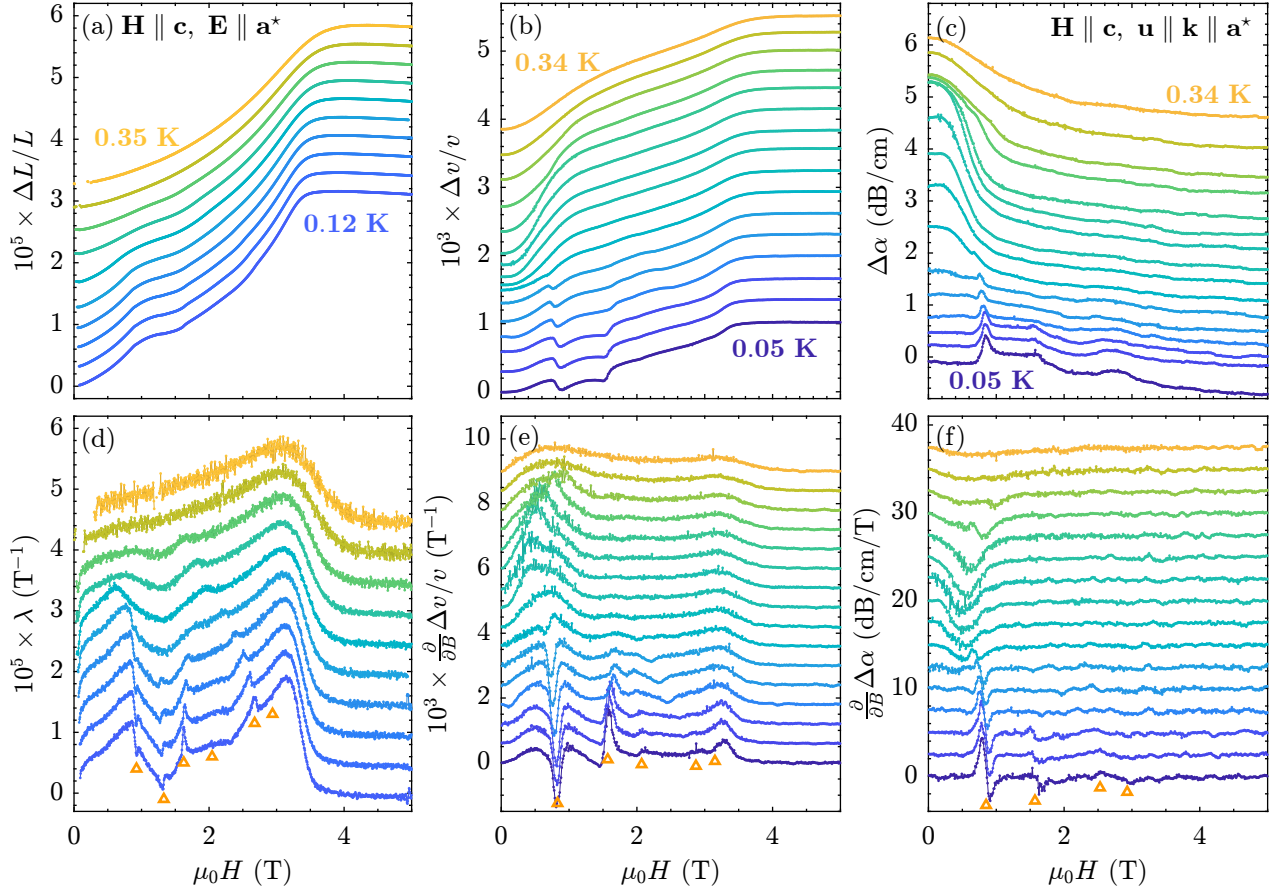


FIG. 7. Field-induced magnetoelastic changes (top panels) and their numerical derivatives (bottom) for $\mathbf{H} \parallel \mathbf{c}$ configuration. We show magnetostrictive changes in sample dilation (a), sound velocity (b) and attenuation (c) in the triangular plane. Various transition fields and measurement temperatures are indicated in the figure. Curves at different temperatures are offset for visibility.

convex up to saturation. In this regime, the magnetization reaches exactly one third of its saturation value $M_{\text{sat}} = 1.29(1) \mu_B/\text{Ru}^{3+}$, corroborating our identification as a $m = 1/3$ magnetization plateau. Interestingly, the magnetostriction $\Delta l(H)/l$ [see Fig. 7(a)] seems to mimic the magnetization curve in the entire field range. This gives credence to the exchange-striction picture discussed above, in which the sample dilation would simply mimic the magnetic bond energies along the probing direction, i.e. $\Delta l/l \sim \frac{g\Lambda_1}{k} \sum_{\langle ij \rangle \parallel \mathbf{a}^*} \langle \hat{\mathbf{S}}_i \cdot \hat{\mathbf{S}}_j \rangle$ where k is a stiffness constant. Finally, we remark on the cusp in magnetization at H_{sat} : The latter appears to be rounded significantly more than the $2k_B T \sim 0.1$ T expected from thermal broadening. Such behavior is typical of broken $SU(2)$ symmetry in spin-orbit coupled systems, perhaps hinting at the presence of some non-trivial anisotropy terms [51].

E. Neutron Diffraction

We carried out single-crystal neutron diffraction experiments to investigate the magnetic order realized

across the entire phase diagram in $\mathbf{H} \parallel \mathbf{c}$ orientation, the results of which are summarized in Fig. 9. As above, we start from the simplest phase, the collinear magnetization plateau. At $\mu_0 H = 1.5$ T we observe sharp magnetic Bragg peaks with a power-law onset of the order parameter below ~ 0.29 K [see Fig. 9(m)], broadly consistent with the $2\beta \approx 0.7$ exponent expected for 3D XY universality. The propagation vector is $\mathbf{q} = (1/3, 1/3, 1/2)$, pointing to an antiferromagnetic nearest neighbor inter-plane coupling $J_c > 0$ [Fig. 9(c)]. Additional reflections are visible in the $l = 0$ plane, corresponding to the second harmonic $2\mathbf{q} \equiv (1/3, 1/3, 0)$ [Fig. 9(h)]. Due to the non-bipartite nature of the three-sublattice order on the triangular lattice, J_c is frustrated by the field, which prefers to cant *all* layers towards $\mathbf{H} \parallel \mathbf{c}$. We're left with a mixed FM-AFM inter-layer stacking involving the tree Fourier components \mathbf{q} , $2\mathbf{q}$ and $\mathbf{k} = 0$ (i.e. the uniform magnetization), all of which are necessary to construct a semi-classical equal moment structure.

Towards lower fields, there is a commensurate-incommensurate lock-in transition at $\mu_0 H_c \approx 0.95$ T. Below this point, the magnetic Bragg peaks split into sets of three incommensurate (IC) reflections, equally spaced

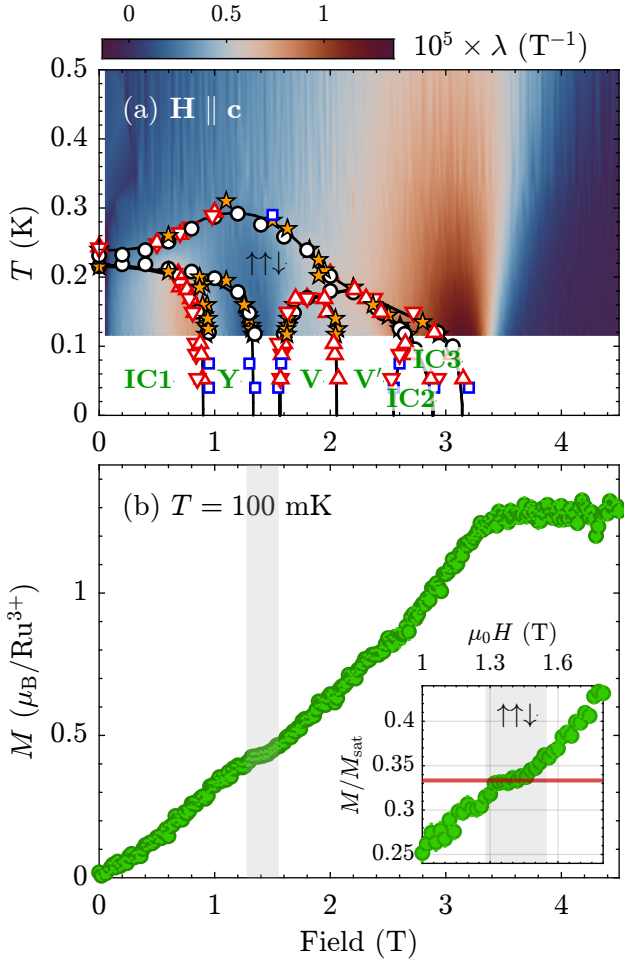


FIG. 8. (a) Magnetic phase diagram of $(\text{CD}_3\text{ND}_3)_2\text{NaRuCl}_6$ for the $\mathbf{H} \parallel \mathbf{c}$ field direction. Color indicates the magnetostriction coefficient $\lambda(H)$. White circles represent lambda anomalies from heat capacity. Orange stars are transitions extracted from magnetostriction. Red triangles (up/down facing) indicate anomalies in sound velocity and attenuation. Blue squares are transitions seen in neutron diffraction. (b) Magnetization curve along $\mathbf{H} \parallel \mathbf{c}$ at $T = 100$ mK, measured with the Faraday balance technique. The inset shows a zoom-in on the “ $\uparrow\downarrow$ ”-phase, displaying a plateau at one third of the saturation magnetization.

around the H and K-points [Fig.9(a,b,f,g)]. They move along the edges of the Brillouin zone, reaching $\mathbf{Q}_1 \approx (0.35, 0.35, l)$, $\mathbf{Q}_2 \approx (0.3, 0.35, l)$ and $\mathbf{Q}_3 \approx (0.35, 0.3, l)$ towards zero field. Note the intensity in both $l = 1/2$ and $l = 0$ planes, where the latter are no longer harmonics, but belong to a distinct secondary \mathbf{q} -vector. This is rather unusual given the direct AA-stacking geometry, perhaps hinting at some exchange anisotropy or further neighbor coupling between triangular planes. Both adopt the exact same IC shift, clearly indicating that these are Fourier components present in the same magnetic phase. The satellites around each commensurate position can be generated by applying three-fold rotations to a propagation vector $\mathbf{q}_{\text{IC}} = (1/3 + \delta, 1/3 + \delta, q_c)$

where $\delta(H)$ is the field-dependent IC shift [Fig.9(k)], resulting in $(1/3 - 2\delta, 1/3 + \delta, q_c)$ and $(1/3 + \delta, 1/3 - 2\delta, q_c)$. These three reciprocal lattice points are equivalent in the paramagnetic phase. Therefore, the zero-field ground state may be either a complex six- \mathbf{q} magnetic order or a two- \mathbf{q} structure with a trivial population of three-fold degenerate domains. We detect no changes in scattering intensity upon employing a field cooling or zero-field cooling protocol.

In the high-field limit, we observe a similar C-IC transition. The commensurate $l = 1/2$ peaks seen in the $m = 1/3$ plateau gradually lose intensity and disappear completely above 2.6 T. This leaves only the $l = 0$ reflections which move away from the K-point, resulting in a long-period incommensurate structure with simple ferromagnetic inter-plane stacking [Fig.9(d,e,i,j)]. We clearly observe *two* distinct IC presaturation phases: First the peaks shift towards the M points, then around 2.9 T the trend reverses and the ordering vector moves towards Γ . Note that in these high-field phases, only one satellite remains around each commensurate position, indicating a simple single- \mathbf{q} magnetic order.

F. Inelastic Neutron Scattering

In Fig. 10 we present the magnetic excitation spectrum of $(\text{CD}_3\text{ND}_3)_2\text{NaRuCl}_6$ in the triangular ($hk0$) plane, obtained from single-crystal neutron spectroscopy in the $\mathbf{H} \parallel \mathbf{c}$ field-polarized regime at $\mu_0 H = 7$ T. As expected, there is one resolution-limited spin-wave branch with a bandwidth $9JS \approx 0.50$ meV. The spin-gap $\Delta = 0.58(1)$ meV to the lowest excitation at the K-point is in excellent agreement with the value $\Delta = g_c \mu_B \mu_0 (H - H_{\text{sat}}) = 0.591(8)$ meV expected from ESR and thermodynamics.

Spin-wave theory is exact for the fully polarized ferromagnet [52], so a fit to the extracted dispersion relation $\hbar\omega_{\mathbf{Q}}$ may be used to determine the leading terms in the low-energy effective spin Hamiltonian. Since the g -factor and external field are known to high precision, we keep the Zeeman term fixed throughout this procedure. The data are well described by a simple nearest neighbor Heisenberg triangular lattice model with $J = 1.32(1)$ K (Fig. 10(g), green line). Potential further neighbor interactions J_2 or J_3 do not improve the fit and can be excluded at the $\sim 2\%$ level. We cannot probe the inter-plane couplings directly due to the scattering geometry ($hk0$) in this experiment. However, the classical saturation field $\mu_0 H_{\text{sat}} = 9JS/g_c \mu_B = 3.29(4)$ T nicely matches the $\mu_0 H_{\text{sat}} = 3.20(5)$ T observed experimentally. This places strong constraints on the leading AFM inter-plane coupling J_c . We estimate $J_c \lesssim 0.1J$, clearly pointing to a quasi-2D system.

Given the spin-orbital entangled wavefunctions, we also attempt to fit a more general anisotropic Hamil-

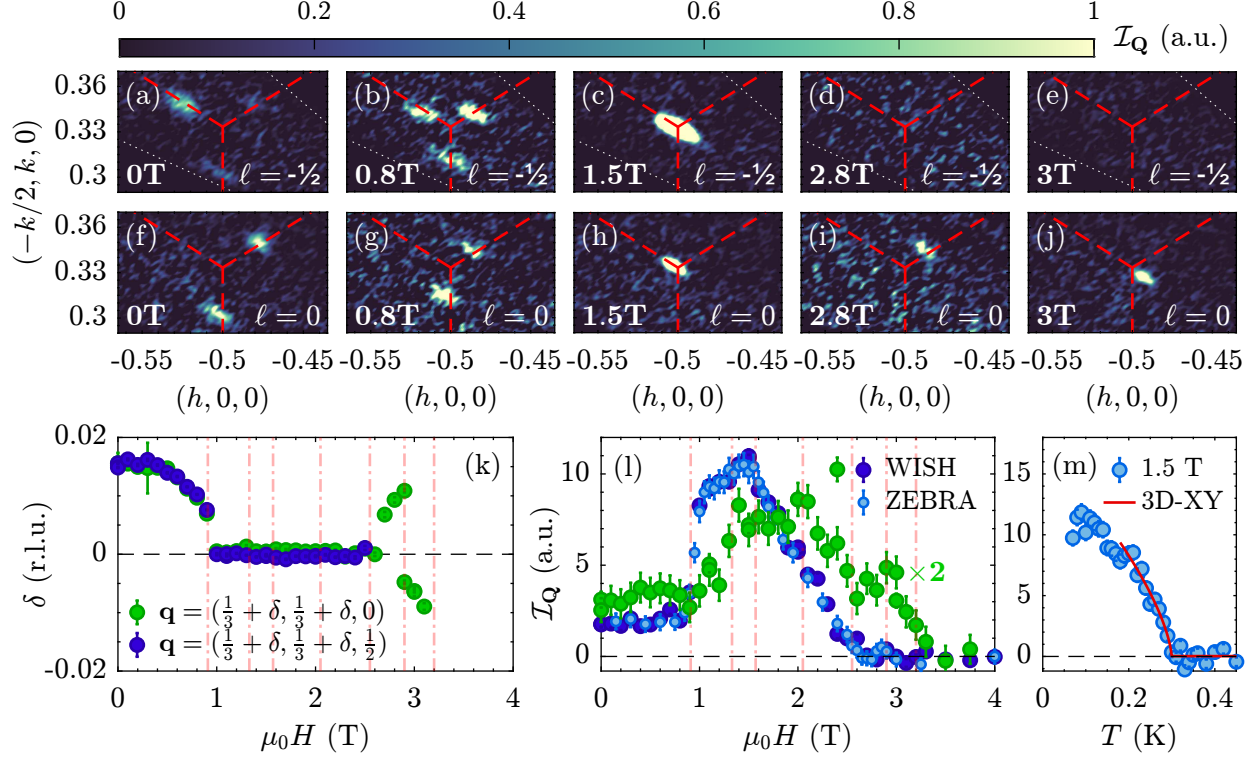


FIG. 9. Neutron diffraction in $(\text{CD}_3\text{ND}_3)_2\text{NaRuCl}_6$ for longitudinal fields $\mathbf{H} \parallel \mathbf{c}$. Elastic scattering intensity near the H-point (a-e) and K-point (f-j) for various magnetic field strengths. A paramagnetic background taken at $T = 0.5$ K is subtracted point-by-point from all panels. Red lines indicate the Brillouin zone boundaries. (k) Field-dependent incommensurability $\delta(H)$ and (l) integrated intensity for both types of ordering vectors. Vertical lines denote the transition fields from Fig. 8(a). (m) Order parameter against temperature in the magnetization plateau phase at $\mu_0 H = 1.5$ T.

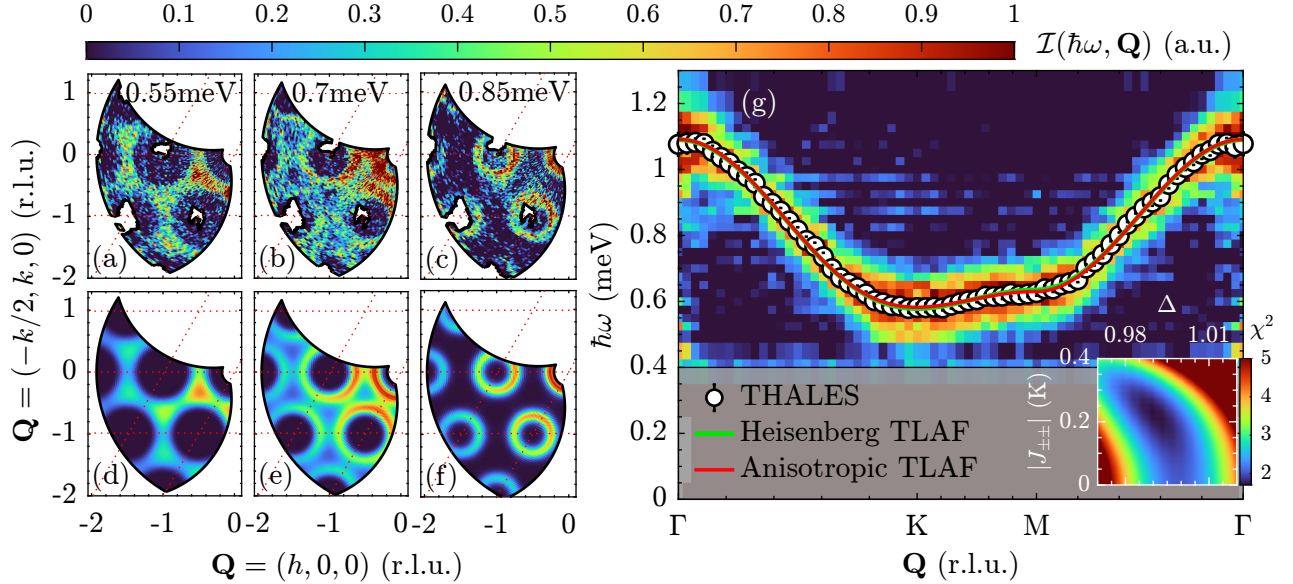


FIG. 10. Inelastic spectra of $(\text{CD}_3\text{ND}_3)_2\text{NaRuCl}_6$ in the fully polarized state at $\mu_0 H = 7$ T. (a-c) False color plots of INS intensity for 2D slices in momentum space taken at various constant energies. Spurions from Bragg peaks re-scattered inelastically are masked out. (d-f) Simulated LSWT intensity in the same range using Eq. 2, convoluted with experimental resolution and form factor. (g) Dispersion relation along high symmetry directions. Markers show extracted peak positions, green/red lines are fits to a 2D Heisenberg/anisotropic model discussed in the text. Inset shows the χ^2 loss function for anisotropic exchange parameters in the fit to Eq. 2.

tonian

$$\hat{\mathcal{H}} = \sum_{\langle ij \rangle} J(S_i^x S_j^x + S_i^y S_j^y + \Delta S_i^z S_j^z) \quad (2)$$

$$+ 2J_{\pm\pm}[(S_i^x S_j^x - S_i^y S_j^y)c_\alpha - (S_i^x S_j^y + S_i^y S_j^x)s_\alpha]$$

$$+ J_{z\pm}[(S_i^y S_j^z + S_i^z S_j^y)c_\alpha - (S_i^x S_j^z + S_i^z S_j^x)s_\alpha].$$

where $c(s)_\alpha = \cos(\sin)\varphi_\alpha$. Here the phases $\varphi_\alpha \in (0, 2\pi/3, 4\pi/3)$ associated with the translation vectors $\mathbf{a}, \mathbf{b}, \mathbf{a} + \mathbf{b}$ give rise to a bond dependence on the pseudo-dipolar couplings $J_{\pm\pm}$ and $J_{z\pm}$. In practice, we are not sensitive to $J_{z\pm}$, as it only enters the dispersion relation for a finite in-plane magnetic moment. This model results in a marginally better fit ($\chi^2 \approx 1.7$ vs. $\chi^2 \approx 2$), with $J = 1.31(2)$ K, $\Delta = 1.00(2)$ and $|J_{\pm\pm}| = 0.31_{-0.23}^{+0.12}$ K. The system is clearly Heisenberg-like, with no signs of XXZ anisotropy. Our data do favor a strong $J_{\pm\pm}$ term but with significant uncertainties, leaving neither one of the bond dependent terms well constrained. We leave this issue to future investigations in a transverse-field geometry [10].

II. DISCUSSION

The novel quantum material $(\text{CD}_3\text{ND}_3)_2\text{NaRuCl}_6$ exhibits a perfect triangular lattice of Ru^{3+} ions realizing the spin-orbital entangled $j_{\text{eff}} = 1/2$ state. Perhaps its most striking property is the highly complex phase diagram in $\mathbf{H} \parallel \mathbf{c}$ composed of seven distinct spin states, three of which are incommensurate with the lattice. The spin Hamiltonian is described at leading order by a purely 2D isotropic Heisenberg model with nearest neighbor coupling $J \approx 1.3$ K. However, in the following we argue for three important perturbations to this picture, which drive the physics, resulting in the rich sequence of field-induced transitions: inter-plane coupling, exchange anisotropy and magnetoelastic effects.

At least the four commensurate states in the center of the phase diagram may be understood semi-classically by considering only the first of these terms, the inter-plane exchange. $(\text{CD}_3\text{ND}_3)_2\text{NaRuCl}_6$ realizes a direct AA-type stacking of triangular planes with an AFM nearest neighbor coupling $J_c \lesssim 0.1J$. Its competition with the magnetic field H results in a mixed FM-AFM inter-layer pattern which contains both $\mathbf{q} = (1/3, 1/3, 1/2)$ and $2\mathbf{q}$ Fourier components. In Fig. 11 we sketch the proposed spin configurations in these phases, obtained through classical energy minimization of all possible six-sublattice groundstates with real-space perturbation corrections to model the effects of quantum order-by-disorder [36]. The simplest is the $m = 1/3$ magnetization plateau, a collinear state forming alternating layers of $\uparrow\uparrow\downarrow$ and $\uparrow\downarrow\uparrow$ moments. This is followed by the well-known “Y” and “V” phases at slightly lower/higher fields, where the finite J_c results in an AFM canting of the in-plane spin components. Finally, a fourth phase is generally expected to arise in AA-stacked triangular

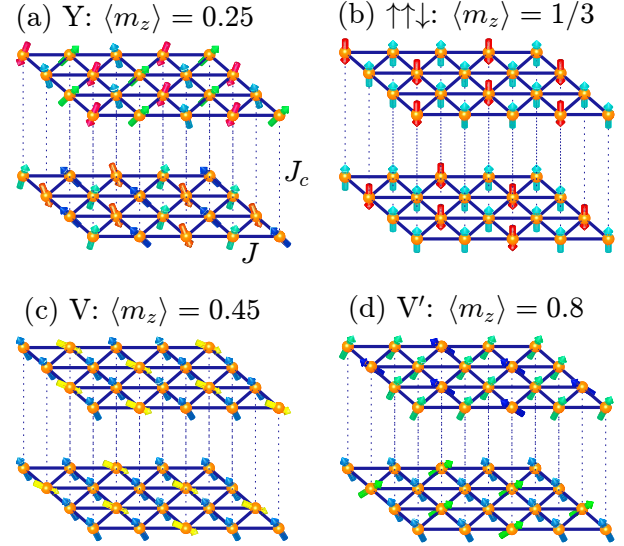


FIG. 11. Sketch of the proposed magnetic structures in the four commensurate phases (a) Y, (b) $\uparrow\uparrow\downarrow$, (c) V and (d) V'.

lattice magnets with $J_c > 0$, often labeled “V” [53, 54]. It is a simple consequence of the J_c vs. H competition, which favors a different inter-plane stacking close to the plateau and near saturation: In the former case the choice of minority spin is staggered between layers, whereas in the latter it is not. A first-order transition between these states is predicted at $H_c \approx 0.7H_{\text{sat}}$ in the Heisenberg limit [53], only weakly depending on J_c . This is in good agreement with the $H_c \approx 2.1$ T (corresponding to $\sim 0.65H_{\text{sat}}$) seen in experiment. An analogous transition has been identified in $\text{Ba}_3\text{CoSb}_2\text{O}_9$ [55, 56], the closest proxy to an ideal Heisenberg triangular lattice antiferromagnet known to date.

Let us turn to the IC behavior observed towards the edges of the phase diagram: The \mathbf{q} -vector realized in zero field cannot be explained by a Heisenberg model on a perfect triangular lattice [36] and necessarily imposes some in-plane anisotropy term, either in spin-space or in real space. The simplest possibility would be a structural transition, giving rise to a “static” $J - J'$ isosceles distortion of the triangular plane that discriminates between chain-like J and zig-zag J' interactions. This model has been discussed thoroughly in the literature [57–59], mostly in the context of the distorted triangular lattice magnets Cs_2CuCl_4 [60, 61], Cs_2CuBr_4 [62, 63] or $\text{Ca}_3\text{ReO}_5\text{Cl}_2$ [64, 65]. But a “clean” experimental realization in the limit $(J' - J) \ll J$ has not been reported to date. The classical energy is minimized by a propagation vector $q_{\text{IC}} = \cos^{-1}(-J'/2J)/2\pi$, resulting in an IC spiral groundstate with three degenerate structural domains. After accounting for quantum renormalization, the detected $q_{\text{IC}} \approx 0.35$ r.l.u. would correspond to an exchange ratio of $J'/J \approx 1.06$ [66–68]. The expected $H - T$ phase diagram [57–59] looks strikingly similar to experiment, with IC states towards the edges and the typical commensurate Y/UUD/V phases in the center,

where order-by-disorder selection is strongest.

However, this option is ruled out by experiment: $(\text{CD}_3\text{ND}_3)_2\text{NaRuCl}_6$ *does* go through a structural transition at $T^* \approx 118$ K, but our single-crystal x-ray diffraction data clearly establish that three-fold symmetry (i.e. $J' = J$) remains intact, at least down to T_N [36]. Instead, we point out two alternative mechanisms which could account for the IC behavior, both of which rely on the strong spin-orbit effects.

An obvious culprit would be the magnetoelastic coupling. The latter could drive a magneto-structural phase transition at T_{N2} , resulting in a “dynamic” $J - J'$ isosceles distortion depending on both field and temperature. Such effects are often seen in pyrochlore systems like CdCr_2O_4 or HgCr_2O_4 (cf. “Spin-Peierls” effect [69, 70]), where a *linear* gain in exchange energy upon distorting the lattice always leads to a small deformation below T_N . There are two issues with this approach: Firstly, the strains $\Delta l/l \lesssim 10^{-5}$ seen in dilatometry are three orders of magnitude smaller than the shift δ of the incommensurate Bragg peaks. Furthermore, the leading correction to the classical energy $\Delta E \approx -\frac{9}{8}JS^2\varepsilon_m^2$ for a monoclinic lattice strain ε_m is *quadratic* [36], so this argument does not easily generalize to the 2D triangular lattice.

One could potentially salvage this by invoking the pseudo Jahn-Teller effect in the presence of strong SOC, which was recently proposed in $5d^5$ iridate perovskites to explain a small tetragonal distortion below T_N [71]. Lattice deformations will modulate the spatial shape of the spin-orbital wavefunctions, which can generate new terms $\delta\mathcal{H}_{ij} \sim g_\gamma\varepsilon_\gamma Q_{ij}^\gamma$ in the Hamiltonian, describing the pseudospin-lattice coupling between two-site quadrupoles $Q_{ij}^\gamma \sim \hat{S}_i^\alpha \hat{S}_j^\beta$ of the appropriate symmetry and strains ε_γ . An extension of this effect to the triangular lattice geometry would be an interesting problem to tackle theoretically.

In any such magnetoelastic scenario, the $J - J'$ anisotropy and the IC splitting of the \mathbf{q} -vector must both follow the order parameter. This would imply $q_{\text{IC}} \rightarrow 1/3$ as we approach $T \rightarrow T_{N2}$ at low fields, but also in the limit $H \rightarrow H_{\text{sat}}$. The latter prediction is in direct conflict with our diffraction results. In the high-field “IC3” pre-saturation phase, q_{IC} moves *away* from the commensurate position even as the magnetic Bragg peak intensity goes to zero [see Fig. 9(k,l)], making for a strong argument against the magnetoelastic mechanisms discussed above. Another important clue comes from the relative intensities of zero-field magnetic satellites near the K-points [see Fig. 9(f)]. We have confirmed for all reflections in the family $\mathbf{Q} = (1/3, 1/3, 0) + \delta$, that those with IC shift $\delta \parallel \mathbf{Q}$ - that is $\mathbf{Q} \approx (0.35, 0.35, 0)$ and six-fold equivalents - carry no intensity, indicating an effect of the neutron polarization factor. This is inconsistent with a simple coplanar spiral structure with multiple domains, favoring instead a multi- \mathbf{q} order incorporating several longitudinal spin density wave contributions.

Bond-dependent exchange anisotropy presents a simple alternative to stabilize an incommensurate structure.

Specifically, the Heisenberg-Kitaev model on a triangular lattice has been predicted to realize the so called \mathbb{Z}_2 vortex crystal [17, 25, 30]. Even for a tiny Kitaev-term $|K| \ll J$, the Fourier transformed exchange matrix is minimized by three different ordering vectors

$$\mathbf{q}_{\text{IC}} = \hat{\mathbf{e}}^\gamma \left| 1 - \frac{1}{\pi} \cos \left(\frac{J}{2(J+K)} \right) \right|, \quad (3)$$

one for each spin component $\gamma \in (x, y, z)$. Locally, the magnetic structure would still mimic the typical 120° order. But on larger length scales, we would see a superlattice of topological defects - \mathbb{Z}_2 vortices - which crystallize into a triangular arrangement. This structure has three main \mathbf{q} -vectors, preserving three-fold symmetry, but with many higher harmonics to retain a uniform moment size. Since the bond-dependent terms break all continuous symmetries, the groundstate also acquires a finite spin-gap Δ [17], seemingly consistent with our heat capacity measurements indicating $\Delta \sim 0.4J$.

In practice, the presence of a small Kitaev term in $(\text{CD}_3\text{ND}_3)_2\text{NaRuCl}_6$ should not be surprising. Bond dependent exchange anisotropies in the parallel-edge superexchange geometry have been proposed by several authors [14, 25, 26]. Given the bond angles deviating from 90° and the significant trigonal distortion $\Delta/\lambda \simeq -0.5$, we expect such terms to be sub-leading compared to J [41]. However, the observed propagation vector $q_{\text{IC}} \approx 0.35$ r.l.u. can be generated by a modest ferromagnetic Kitaev term $K \sim -0.1J$, which seems completely realistic. In fact, the contribution from $J_{\pm\pm}$ alone obtained through INS in the polarized regime would be significantly larger, with $K = -2J_{\pm\pm}$ amounting to $K/J \approx -0.4_{-0.2}^{+0.3}$. This makes $(\text{CD}_3\text{ND}_3)_2\text{NaRuCl}_6$ a leading candidate to realize the \mathbb{Z}_2 vortex crystal phase. Given the large uncertainties on $J_{\pm\pm}$ and completely undetermined $J_{z\pm}$, more work should be put towards constraining these bond anisotropies. We note that the stability of this phase against finite inter-plane coupling J_c , anisotropies away from the Heisenberg-Kitaev limit $J_{z\pm} \neq 2\sqrt{2}J_{\pm\pm}$, or magnetic field H have not been investigated theoretically, likely due to the inherent complexity of the vortex crystal state. All of these problems would be of imminent interest in understanding the groundstate of $(\text{CD}_3\text{ND}_3)_2\text{NaRuCl}_6$.

Finally, we comment on the tunability of this new structural archetype MA_2ARuX_6 . Powder samples of several different members in this family have been previously synthesized in [35], confirming that at least the alkali A and halide X can easily be replaced. This already gives huge flexibility in tuning the magnetism of these exciting new quantum materials. Especially the hierarchy between the small perturbing terms like inter-plane interactions, bond anisotropies or magnetoelastic coupling may be easily modified by changing the anions participating in superexchange.

III. CONCLUSION

The new quantum antiferromagnet $(\text{CD}_3\text{ND}_3)_2\text{NaRuCl}_6$ poses a rare model system to combine the effects of strong spin-orbit coupling endemic to $4d/5d$ transition metals and the geometric frustration on a triangular lattice. Its magnetism is described by a quasi-2D nearest-neighbor Heisenberg Hamiltonian with the addition of inter-plane interactions, bond anisotropies and magnetoelastic coupling as small perturbing terms, begetting an extremely rich phase diagram including several incommensurate states. Of particular interest is the multi- \mathbf{q} ground state realized in zero magnetic field, posing a prime candidate to host the exotic \mathbb{Z}_2 vortex crystal phase. This calls for polarized diffraction studies to confirm the explicit spin configuration and spectroscopy experiments to investigate its dynamics. $(\text{CD}_3\text{ND}_3)_2\text{NaRuCl}_6$ constitutes the first member in a large family of $4d/5d$ -based quantum triangular lattice magnets, opening new pathways to study the interplay between geometric frustration and spin-orbit effects.

ACKNOWLEDGMENTS

This work is supported by a MINT grant of the Swiss National Science Foundation. We acknowledge the support of the HLD at HZDR, member of the European Magnetic Field Laboratory (EMFL), and the Würzburg-Dresden Cluster of Excellence on Complexity and Topology in Quantum Matter - ct.qmat (EXC 2147, project ID 390858490). We also thank Sergei Zherlytsin (HZDR) for the assistance with ultrasound measurements. We acknowledge the beam time allocation at ISIS (WISH id: RB2420060 [72]), PSI (ZEBRA id: 20240853) and ILL (THALES id: 4-01-1857 [73]).

Appendix A: Methods

Single crystal samples of $(\text{CD}_3\text{ND}_3)_2\text{NaRuCl}_6$ were grown using a hydrothermal method analogous to [35]. We obtain dark red crystals with highly symmetric hexagonal faces and typical sample mass of order 10–200 mg. Fully deuterated ($\geq 98\%$ D) precursors were employed in the growth to limit the incoherent H-scattering in neutron experiments. The structure and sample quality of all experimental probes was confirmed using a Bruker APEX-II single-crystal x-ray diffractometer. Detailed refinements to characterize the low-temperature structural transition were carried out at the I19 synchrotron beamline (Diamond, UK). Datasets of $1\text{--}5 \times 10^4$ reflections were collected at $\lambda = 0.689 \text{ \AA}$ on several $\sim 50 \mu\text{m}$ single crystal samples between $T = 150 \text{ K}$ and 30 K . The *shelx* software suite [74] was employed for the refinements.

Magnetic susceptibility on a $m = 20 \text{ mg}$ single crystal

were performed in a commercial Magnetic Property Measurements System (MPMS) SQUID magnetometer in a $\mu_0 H = 0.1 \text{ T}$ probing field. High- T magnetization curves up to $\mu_0 H = 7 \text{ T}$ were collected in the same configuration. The magnetization data at dilution temperatures were obtained on a 2 mg sample using a home-built Faraday balance setup [50] and calibrated to absolute units using the SQUID data at 2 K as reference. For the ESR experiments a tunable-frequency spectrometer (similar to the one described in Ref. [75]) was employed, equipped with a 16 T superconducting magnet. VDI microwave-chain sources (product of Virginia Diodes, Inc., USA) were used to generate radiation in the frequency range of 50–360 GHz. A hot-electron n-InSb bolometer (product of QMC Instruments Ltd., UK), operated at 4.2 K, was employed as a THz detector. For the frequencies below 50 GHz a microwave vector network analyser (MVNA, production of AB Millimeter, France) was used. Sample holders in the Faraday and Voigt configuration were used for $\mathbf{H} \parallel \mathbf{c}$ and $\mathbf{H} \parallel \mathbf{a}$ measurements respectively. 2,2-diphenyl-1-picrylhydrazyl (DPPH) was used as a standard frequency-field marker. The heat capacity of a 0.4 mg single crystal sample was measured with the standard relaxation calorimetry technique on a 9 T Physical Property Measurement System (PPMS) with a ^3He - ^4He dilution refrigerator insert. Magnetostriction data were taken in the same configuration using a $L = 1.48 \text{ mm}$ long single crystal with natural faces in the (100) and (001) cleavage planes. The sample dilation was determined with a miniature capacitive dilatometer [76] in conjunction with an Andeen-Hagerling 2700A bridge, operated at 1.11 kHz. Sound velocity measurements of the longitudinal c_{11} mode (polarization \mathbf{u} and propagation \mathbf{k} along the \mathbf{a}^* -axis) were carried out at the Dresden High Magnetic Field Laboratory using a pulse-echo method with phase-sensitive detection [77, 78]. LiNbO_3 transducers were bonded with Thiokol to two parallel (100) faces of a $L = 2.8 \text{ mm}$ long single crystal sample. Experiments were carried out at $f = 40 \text{ MHz}$ using a ^3He - ^4He dilution refrigerator equipped with an 18 T magnet.

Single-crystal neutron diffraction experiments were performed at WISH (ISIS, UK) [72] and ZEBRA (PSI, Switzerland) on the same $m = 55 \text{ mg}$ sample aligned in the $(hk0)$ scattering plane. The crystal was mounted in a ^3He - ^4He dilution refrigerator together with a 10 T (6 T) vertical cryomagnet. A constant wavelength $\lambda = 1.383 \text{ \AA}$ (Ge monochromator) was chosen for the latter experiment. The incommensurate positions and intensities from WISH were extracted by fitting 2D Gaussian profiles with a fixed resolution ($\Delta q_{\parallel}, \Delta q_{\perp}$) to the data. These data were analyzed using the mantid software suite [79].

Inelastic neutron scattering experiments were carried out on the cold triple-axis spectrometer THALES (ILL, France) [73] with Flatcone multi-analyzer setup. 16 single crystals were coaligned in the ab scattering plane for a total sample mass of $m \simeq 1.9 \text{ g}$. The probe was installed with $(hk0)$ scattering geometry in a dilution refrigerator with 10 T vertical cryomagnet and cooled to

$T \sim 70$ mK. All measurements were taken at a final energy $E_f = 4.06$ meV (FWHM resolution $\Delta E \approx 175 \mu\text{eV}$), fixed by the Flatcone setup. 35 constant-energy slices were collected in the field-polarized regime at $\mu_0 H = 7$ T, rotating 90° through the scattering plane in 0.5° steps. To reconstruct the spin-wave dispersion relation, spurions from inelastically re-scattered Bragg peaks were masked, a constant background was subtracted, the data were normalized by form factor and averaged over > 20 equivalent paths through several Brillouin zones. The SpinW software [80] was employed for the spin-wave intensity calculations.

Appendix B: Data Availability

All data are available upon reasonable request to the corresponding author. The neutron scattering data collected at WISH (STFC ISIS Neutron and Muon Source) and THALES (Institut Laue-Langevin) are available at <https://doi.org/10.5286/ISIS.E.RB2420060> and <https://doi.ill.fr/10.5291/ILL-DATA.4-01-1857>, respectively.

Appendix C: Author Contributions

Samples used in this study were grown by J.N. and Z.Y. Magnetometry and dilatometry studies were car-

ried out by J.N. and S.G. Heat capacity measurements were performed by J.N., B.D. and S.G. ESR measurements were performed by K.Y.P. and S.A.Z., while ultrasound data were collected by K.Y.P., J.S., B.V.S. and F.H. Neutron diffraction experiments at WISH and ZEBRA were carried out by J.N. and A.Z. with assistance of D.K., P.M., F.O. and O.Z. respectively. INS measurements at THALES were taken by J.N., S.G. and A.Z. with assistance from P.S. and A.H. Synchrotron x-ray experiments at I19 were performed by J.N., S.G. and A.Z. with assistance from D.A. and S.B. Analysis and modeling of experimental data was carried out by J.N. The manuscript was written by J.N. and A.Z. with input from all coauthors.

Appendix D: Competing Interests

The authors declare no competing interests.

-
- [1] G. H. Wannier, Antiferromagnetism. The Triangular Ising Net, *Physical Review* **79**, 357 (1950).
 - [2] L. Balents, Spin liquids in frustrated magnets, *Nature* **464**, 199 (2010).
 - [3] C. Lacroix, P. Mendels, and F. Mila, eds., *Introduction to Frustrated Magnetism: Materials, Experiments, Theory*, 1st ed., Springer Series in Solid-State Sciences, Vol. 164 (Springer, Berlin, 2011).
 - [4] A. L. Chernyshev and M. E. Zhitomirsky, Spin waves in a triangular lattice antiferromagnet: Decays, spectrum renormalization, and singularities, *Physical Review B* **79**, 144416 (2009).
 - [5] S. Ito, N. Kurita, H. Tanaka, S. Ohira-Kawamura, K. Nakajima, S. Itoh, K. Kuwahara, and K. Kakurai, Structure of the magnetic excitations in the spin-1/2 triangular-lattice Heisenberg antiferromagnet $\text{Ba}_3\text{CoSb}_2\text{O}_9$, *Nature Communications* **8**, 1 (2017).
 - [6] T. Xie, A. A. Eberharter, J. Xing, S. Nishimoto, M. Brando, P. Khanenko, J. Sichelschmidt, A. A. Turini, D. G. Mazzone, P. G. Naumov, L. D. Sanjeewa, N. Harrison, A. S. Sefat, B. Normand, A. M. Läuchli, A. Podlesnyak, and S. E. Nikitin, Complete field-induced spectral response of the spin-1/2 triangular-lattice antiferromagnet CsYbSe_2 , *npj Quantum Materials* **8**, 1 (2023).
 - [7] Y. Li, P. Gegenwart, and A. A. Tsirlin, Spin liquids in geometrically perfect triangular antiferromagnets, *Journal of Physics: Condensed Matter* **32**, 224004 (2020).
 - [8] P. A. Maksimov, Z. Zhu, S. R. White, and A. L. Chernyshev, Anisotropic-Exchange Magnets on a Triangular Lattice: Spin Waves, Accidental Degeneracies, and Dual Spin Liquids, *Physical Review X* **9**, 21017 (2019).
 - [9] M. Zhu, L. M. Chinellato, V. Romerio, N. Murai, S. Ohira-Kawamura, C. Balz, Z. Yan, S. Gvasaliya, Y. Kato, C. D. Batista, and A. Zheludev, Wannier states and spin supersolid physics in the triangular antiferromagnet $\text{K}_2\text{Co}(\text{SeO}_3)_2$, *npj Quantum Materials* **10**, 74 (2025).
 - [10] L. Woodland, R. Okuma, J. R. Stewart, C. Balz, and R. Coldea, From continuum excitations to sharp magnons via transverse magnetic field in the spin- $\frac{1}{2}$ ising-like triangular lattice antiferromagnet $\text{Na}_2\text{BaCo}(\text{PO}_4)_2$, *Phys. Rev. B* **112**, 104413 (2025).
 - [11] A. O. Scheie, Y. Kamiya, H. Zhang, S. Lee, A. J. Woods, M. O. Ajeesh, M. G. Gonzalez, B. Bernu, J. W. Villanova, J. Xing, Q. Huang, Q. Zhang, J. Ma, E. S. Choi, D. M. Pajerowski, H. Zhou, A. S. Sefat, S. Okamoto, T. Berlijn, L. Messio, R. Movshovich, C. D. Batista, and D. A. Tennant, Nonlinear magnons and exchange Hamiltonians of the delafossite proximate quantum spin liquid candidates KYbSe_2 and NaYbSe_2 , *Physical Review B* **109**, 014425 (2024).
 - [12] Z. Zhu, P. A. Maksimov, S. R. White, and A. L. Chernyshev, Disorder-Induced Mimicry of a Spin Liquid in YbMgGaO_4 , *Physical Review Letters* **119**, 157201 (2017).

- [13] G. Jackeli and G. Khaliullin, Mott Insulators in the Strong Spin-Orbit Coupling Limit: From Heisenberg to a Quantum Compass and Kitaev Models, *Physical Review Letters* **102**, 017205 (2009).
- [14] S. Trebst and C. Hickey, Kitaev materials, *Physics Reports* **950**, 1 (2022), kitaev materials.
- [15] Y. Zhou, S. Li, X. Liang, and Y. Zhou, Topological Spin Textures: Basic Physics and Devices, *Advanced Materials* **37**, 2312935 (2025).
- [16] H. Kawamura and S. Miyashita, Phase Transition of the Two-Dimensional Heisenberg Antiferromagnet on the Triangular Lattice, *Journal of the Physical Society of Japan* **53**, 4138 (1984).
- [17] I. Rousochatzakis, U. K. Rössler, J. van den Brink, and M. Daghofer, Kitaev anisotropy induces mesoscopic \mathbb{Z}_2 vortex crystals in frustrated hexagonal antiferromagnets, *Physical Review B* **93**, 104417 (2016).
- [18] T. H. R. Skyrme, A unified field theory of mesons and baryons, *Nuclear Physics* **31**, 556 (1962).
- [19] A. N. Bogdanov and D. A. Yablonskii, Thermodynamically stable “vortices” in magnetically ordered crystals. The mixed state of magnets, *Zh. Eksp. Teor. Fiz* **95**, 178 (1989).
- [20] S. Mühlbauer, B. Binz, F. Jonietz, C. Pfleiderer, A. Rosch, A. Neubauer, R. Georgii, and P. Böni, Skyrmion Lattice in a Chiral Magnet, *Science* **323**, 915 (2009).
- [21] S. Seki, X. Z. Yu, S. Ishiwata, and Y. Tokura, Observation of Skyrmions in a Multiferroic Material, *Science* **336**, 198 (2012).
- [22] A. A. Abrikosov, On the Magnetic Properties of Superconductors of the Second Group, *Sov. Phys. JETP* **5**, 1174 (1957).
- [23] U. Essmann and H. Träuble, The direct observation of individual flux lines in type II superconductors, *Physics Letters A* **24**, 526 (1967).
- [24] H. F. Hess, R. B. Robinson, R. C. Dynes, J. M. Valles, and J. V. Waszczak, Scanning-Tunneling-Microscope Observation of the Abrikosov Flux Lattice and the Density of States near and inside a Fluxoid, *Physical Review Letters* **62**, 214 (1989).
- [25] M. Becker, M. Hermanns, B. Bauer, M. Garst, and S. Trebst, Spin-orbit physics of $j = \frac{1}{2}$ Mott insulators on the triangular lattice, *Physical Review B* **91**, 155135 (2015).
- [26] A. Catuneanu, J. G. Rau, H.-S. Kim, and H.-Y. Kee, Magnetic orders proximal to the Kitaev limit in frustrated triangular systems: Application to $\text{Ba}_3\text{IrTi}_2\text{O}_9$, *Physical Review B* **92**, 165108 (2015).
- [27] Z. Wang, Y. Kamiya, A. H. Nevidomskyy, and C. D. Batista, Three-Dimensional Crystallization of Vortex Strings in Frustrated Quantum Magnets, *Physical Review Letters* **115**, 107201 (2015).
- [28] X. Yao and S. Dong, Stabilization and modulation of the topological magnetic phase with a \mathbb{Z}_2 -vortex lattice in the Kitaev-Heisenberg honeycomb model: The key role of the third-nearest-neighbor interaction, *Physical Review B* **98**, 054413 (2018).
- [29] M. Kishimoto, K. Morita, Y. Matsubayashi, S. Sota, S. Yunoki, and T. Tohyama, Ground state phase diagram of the Kitaev-Heisenberg model on a honeycomb-triangular lattice, *Physical Review B* **98**, 054411 (2018).
- [30] M. Li, N. B. Perkins, and I. Rousochatzakis, Collective spin dynamics of \mathbb{Z}_2 vortex crystals in triangular Kitaev-Heisenberg antiferromagnets, *Physical Review Research* **1**, 013002 (2019).
- [31] S. A. Osorio, M. B. Sturla, H. D. Rosales, and D. C. Cabra, From skyrmions to \mathbb{Z}_2 vortices in distorted chiral antiferromagnets, *Physical Review B* **100**, 220404 (2019).
- [32] E. Seabrook, M. L. Baez, and J. Reuther, \mathbb{Z}_2 vortices in the ground states of classical Kitaev-Heisenberg models, *Physical Review B* **101**, 174443 (2020).
- [33] K. Shinjo, S. Sota, S. Yunoki, K. Totsuka, and T. Tohyama, Density-Matrix Renormalization Group Study of Kitaev-Heisenberg Model on a Triangular Lattice, *Journal of the Physical Society of Japan* **85**, 114710 (2016).
- [34] P. Bhattacharyya, N. A. Bogdanov, S. Nishimoto, S. D. Wilson, and L. Hozoi, NaRuO_2 : Kitaev-Heisenberg exchange in triangular-lattice setting, *npj Quantum Materials* **8**, 1 (2023).
- [35] P. Vishnoi, J. L. Zuo, T. A. Strom, G. Wu, S. D. Wilson, R. Seshadri, and A. K. Cheetham, Structural Diversity and Magnetic Properties of Hybrid Ruthenium Halide Perovskites and Related Compounds, *Angewandte Chemie International Edition* **59**, 8974 (2020).
- [36] See Supplemental Material for further details about the low-temperature crystal structure, the single-ion fitting procedures & ESR data, the magnetoelastic coupling, our inelastic neutron spectroscopy experiment, the proposed magnetic structures, as well as Refs. [81–93].
- [37] A. N. Ponomaryov, L. Zviagina, J. Wosnitza, P. Lampen-Kelley, A. Banerjee, J.-Q. Yan, C. A. Bridges, D. G. Mandrus, S. E. Nagler, and S. A. Zvyagin, Nature of magnetic excitations in the high-field phase of $\alpha\text{-RuCl}_3$, *Phys. Rev. Lett.* **125**, 037202 (2020).
- [38] S. Geschwind and J. P. Remeika, Spin Resonance of Transition Metal Ions in Corundum, *Journal of Applied Physics* **33**, 370 (1962).
- [39] A. Abragam and B. Bleaney, *Electron Paramagnetic Resonance of Transition Ions*, 1st ed., Oxford classic texts in the physical sciences (Oxford University Press, 1970).
- [40] H. Liu, J. Chaloupka, and G. Khaliullin, Exchange interactions in d^5 Kitaev materials: From Na_2IrO_3 to $\alpha\text{-RuCl}_3$, *Physical Review B* **105**, 214411 (2022).
- [41] S. M. Winter, A. A. Tsirlin, M. Daghofer, J. van den Brink, Y. Singh, P. Gegenwart, and R. Valentí, Models and materials for generalized Kitaev magnetism, *Journal of Physics: Condensed Matter* **29**, 493002 (2017).
- [42] A. V. Chubukov and D. I. Golosov, Quantum theory of an antiferromagnet on a triangular lattice in a magnetic field, *Journal of Physics: Condensed Matter* **3**, 69 (1991).
- [43] L. Seabra, T. Momoi, P. Sindzingre, and N. Shannon, Phase diagram of the classical Heisenberg antiferromagnet on a triangular lattice in an applied magnetic field, *Physical Review B* **84**, 214418 (2011).
- [44] D. Yamamoto, G. Marmorini, and I. Danshita, Quantum Phase Diagram of the Triangular-Lattice XXZ Model in a Magnetic Field, *Physical Review Letters* **112**, 127203 (2014).
- [45] M. E. Lines, Elastic properties of magnetic materials, *Physics Reports* **55**, 133 (1979).
- [46] P. C. Hohenberg and B. I. Halperin, Theory of dynamic critical phenomena, *Reviews of Modern Physics* **49**, 435 (1977).
- [47] M. Li, A. Zelenskiy, J. A. Quilliam, Z. L. Dun, H. D. Zhou, M. L. Plumer, and G. Quirion, Magnetoelastic coupling and the magnetization plateau in $\text{Ba}_3\text{CoSb}_2\text{O}_9$,

- Physical Review B **99**, 094408 (2019).
- [48] P. T. Cong, L. Postulka, B. Wolf, N. Van Well, F. Ritter, W. Assmus, C. Krellner, and M. Lang, Magneto-acoustic study near the quantum critical point of the frustrated quantum antiferromagnet Cs_2CuCl_4 , *Journal of Applied Physics* **120**, 142113 (2016).
 - [49] S. K. Thallapaka, B. Wolf, E. Gati, L. Postulka, U. Tutsch, B. Schmidt, P. Thalmeier, F. Ritter, C. Krellner, Y. Li, V. Borisov, R. Valentí, and M. Lang, Magneto-Structural Properties of the Layered Quasi-2D Triangular-Lattice Antiferromagnets $\text{Cs}_2\text{CuCl}_{4-x}\text{Br}_x$ for $x = 0, 1, 2$ and 4 , *Physica Status Solidi (B)* **256**, 1900044 (2019).
 - [50] D. Blosser, L. Facheris, and A. Zheludev, Miniature capacitive Faraday force magnetometer for magnetization measurements at low temperatures and high magnetic fields, *Review of Scientific Instruments* **91**, 73905 (2020), 2002.10168.
 - [51] L. Janssen and M. Vojta, Heisenberg-kitaev physics in magnetic fields, *Journal of Physics: Condensed Matter* **31**, 423002 (2019).
 - [52] R. Coldea, D. A. Tennant, K. Habicht, P. Smeibidl, C. Wolters, and Z. Tylczynski, Direct Measurement of the Spin Hamiltonian and Observation of Condensation of Magnons in the 2D Frustrated Quantum Magnet Cs_2CuCl_4 , *Physical Review Letters* **88**, 4 (2002).
 - [53] D. Yamamoto, G. Marmorini, and I. Danshita, Microscopic Model Calculations for the Magnetization Process of Layered Triangular-Lattice Quantum Antiferromagnets, *Physical Review Letters* **114**, 027201 (2015).
 - [54] M. Li, M. L. Plumer, and G. Quirion, Effects of interlayer and bi-quadratic exchange coupling on layered triangular lattice antiferromagnets, *Journal of Physics: Condensed Matter* **32**, 135803 (2020).
 - [55] K. Okada, H. Tanaka, N. Kurita, D. Yamamoto, A. Matsuo, and K. Kindo, Field-orientation dependence of quantum phase transitions in the $S=1/2$ triangular-lattice antiferromagnet $\text{Ba}_3\text{CoSb}_2\text{O}_9$, *Physical Review B* **106**, 104415 (2022).
 - [56] G. Koutroulakis, T. Zhou, Y. Kamiya, J. D. Thompson, H. D. Zhou, C. D. Batista, and S. E. Brown, Quantum phase diagram of the $S = \frac{1}{2}$ triangular-lattice antiferromagnet $\text{Ba}_3\text{CoSb}_2\text{O}_9$, *Physical Review B* **91**, 024410 (2015).
 - [57] R. Chen, H. Ju, H.-C. Jiang, O. A. Starykh, and L. Balents, Ground states of spin-1/2 triangular antiferromagnets in a magnetic field, *Physical Review B* **87**, 165123 (2013).
 - [58] C. Griset, S. Head, J. Alicea, and O. A. Starykh, Deformed triangular lattice antiferromagnets in a magnetic field: Role of spatial anisotropy and Dzyaloshinskii-Moriya interactions, *Physical Review B* **84**, 245108 (2011).
 - [59] T. Tay and O. I. Motrunich, Variational studies of triangular Heisenberg antiferromagnet in magnetic field, *Physical Review B* **81**, 165116 (2010).
 - [60] R. Coldea, D. A. Tennant, A. M. Tsvelik, and Z. Tylczynski, Experimental Realization of a 2D Fractional Quantum Spin Liquid, *Physical Review Letters* **86**, 1335 (2001).
 - [61] Y. Tokiwa, T. Radu, R. Coldea, H. Wilhelm, Z. Tylczynski, and F. Steglich, Magnetic phase transitions in the two-dimensional frustrated quantum antiferromagnet Cs_2CuCl_4 , *Physical Review B* **73**, 134414 (2006).
 - [62] T. Ono, H. Tanaka, O. Kolomiyets, H. Mitamura, T. Goto, K. Nakajima, A. Oosawa, Y. Koike, K. Kakurai, J. Klenke, P. Smeibidl, and M. Meißner, Magnetization plateaux of the $S = 1/2$ two-dimensional frustrated antiferromagnet Cs_2CuBr_4 , *Journal of Physics: Condensed Matter* **16**, S773 (2004).
 - [63] N. A. Fortune, S. T. Hannahs, Y. Yoshida, T. E. Sherrill, T. Ono, H. Tanaka, and Y. Takano, Cascade of Magnetic-Field-Induced Quantum Phase Transitions in a Spin-1/2 Triangular-Lattice Antiferromagnet, *Physical Review Letters* **102**, 257201 (2009).
 - [64] D. Hirai, T. Yajima, K. Nawa, M. Kawamura, and Z. Hiroi, Anisotropic triangular lattice realized in rhenium oxychlorides $\text{A}_3\text{ReO}_5\text{Cl}_2$ ($A = \text{Ba}, \text{Sr}$), *Inorganic Chemistry* **59**, 10025 (2020), pMID: 32584564.
 - [65] K. Nawa, D. Hirai, M. Kofu, K. Nakajima, R. Murasaki, S. Kogane, M. Kimata, H. Nojiri, Z. Hiroi, and T. J. Sato, Bound spinon excitations in the spin- $\frac{1}{2}$ anisotropic triangular antiferromagnet $\text{Ca}_3\text{ReO}_5\text{Cl}_2$, *Phys. Rev. Res.* **2**, 043121 (2020).
 - [66] Z. Weihong, R. H. McKenzie, and R. R. P. Singh, Phase diagram for a class of spin-1/2 Heisenberg models interpolating between the square-lattice, the triangular-lattice, and the linear-chain limits, *Physical Review B* **59**, 14367 (1999).
 - [67] M. Thesberg and E. S. Sørensen, Exact diagonalization study of the anisotropic triangular lattice Heisenberg model using twisted boundary conditions, *Physical Review B* **90**, 115117 (2014).
 - [68] J. Hasik and P. Corboz, Incommensurate Order with Translationally Invariant Projected Entangled-Pair States: Spiral States and Quantum Spin Liquid on the Anisotropic Triangular Lattice, *Physical Review Letters* **133**, 176502 (2024).
 - [69] K. Penc, N. Shannon, and H. Shiba, Half-Magnetization Plateau Stabilized by Structural Distortion in the Antiferromagnetic Heisenberg Model on a Pyrochlore Lattice, *Physical Review Letters* **93**, 197203 (2004).
 - [70] O. Tchernyshyov, R. Moessner, and S. L. Sondhi, Order by Distortion and String Modes in Pyrochlore Antiferromagnets, *Physical Review Letters* **88**, 067203 (2002).
 - [71] H. Liu and G. Khaliullin, Pseudo-Jahn-Teller Effect and Magnetoelastic Coupling in Spin-Orbit Mott Insulators, *Physical Review Letters* **122**, 057203 (2019).
 - [72] J. Nagl, A. Zheludev, and D. Khalyavin, Field-dependent magnetic structure of the triangular-lattice antiferromagnet $(\text{CD}_3\text{ND}_3)_2\text{NaRuCl}_6$, STFC ISIS Neutron and Muon Source [10.5286/ISIS.E.RB2420060](https://doi.org/10.5286/ISIS.E.RB2420060) (2024).
 - [73] J. Nagl, S. Gvasaliya, A. Zheludev, A. Hiess, and P. Steffens, Excitation spectrum of the triangular-lattice antiferromagnet $(\text{CD}_3\text{ND}_3)_2\text{NaRuCl}_6$, Institut Laue-Langevin (ILL) [10.5291/ILL-DATA.4-01-1857](https://doi.org/10.5291/ILL-DATA.4-01-1857) (2025).
 - [74] G. M. Sheldrick, A short history of SHELX, *Acta Crystallographica Section A* **64**, 112 (2008).
 - [75] S. A. Zvyagin, J. Krzystek, P. H. M. van Loosdrecht, G. Dhalenne, and A. Revcolevschi, High-field ESR study of the dimerized-incommensurate phase transition in the spin-Peierls compound CuGeO_3 , *Physica B* **346-347**, 1 (2004).
 - [76] R. Köchler, R. Wawrzyńczak, H. Dawczak-Dębicki, J. Gooth, and S. Galeski, New applications for the world's smallest high-precision capacitance dilatometer and its stress-implementing counterpart, *Review of Scientific Instruments* **94**, 045108 (2023).

- [77] B. Lüthi, *Physical Acoustics in the Solid State*, 1st ed. (Springer, Berlin, 2005).
- [78] S. Zherlitsyn, S. Yasin, J. Wosnitza, A. A. Zvyagin, A. V. Andreev, and V. Tsurkan, Spin-lattice effects in selected antiferromagnetic materials (review article), *Low Temperature Physics* **40**, 123 (2014).
- [79] O. Arnold, J. C. Bilheux, J. M. Borreguero, A. Buts, S. I. Campbell, L. Chapon, M. Doucet, N. Draper, R. Ferraz Leal, M. A. Gigg, V. E. Lynch, A. Markvardsen, D. J. Mikkelsen, R. L. Mikkelsen, R. Miller, K. Palmen, P. Parker, G. Passos, T. G. Perring, P. F. Peterson, S. Ren, M. A. Reuter, A. T. Savici, J. W. Taylor, R. J. Taylor, R. Tolchenov, W. Zhou, and J. Zikovsky, Mantid—Data analysis and visualization package for neutron scattering and μ SR experiments, *Nuclear Instruments and Methods in Physics Research Section A: Accelerators, Spectrometers, Detectors and Associated Equipment* **764**, 156 (2014).
- [80] S. Toth and B. Lake, Linear spin wave theory for single-Q incommensurate magnetic structures, *Journal of Physics: Condensed Matter* **27**, 166002 (2015).
- [81] A. Wąskowska, L. Gerward, J. Staun Olsen, W. Morgenroth, M. Mączka, and K. Hermanowicz, Temperature- and pressure-dependent lattice behaviour of $\text{RbFe}(\text{MoO}_4)_2$, *Journal of Physics: Condensed Matter* **22**, 055406 (2010).
- [82] Y. Kajita, T. Nagai, S. Yamagishi, K. Kimura, M. Hagihara, and T. Kimura, Ferroaxial Transitions in Glaserite-Type $\text{Na}_2\text{BaM}(\text{PO}_4)_2$ ($\text{M} = \text{Mg}, \text{Mn}, \text{Co}, \text{and Ni}$), *Chemistry of Materials* **36**, 7451 (2024).
- [83] A. J. Hearmon, F. Fabrizi, L. C. Chapon, R. D. Johnson, D. Prabhakaran, S. V. Streltsov, P. J. Brown, and P. G. Radaelli, Electric Field Control of the Magnetic Chiralities in Ferroaxial Multiferroic $\text{RbFe}(\text{MoO}_4)_2$, *Physical Review Letters* **108**, 237201 (2012).
- [84] A. Zelenskiy, J. A. Quilliam, A. Ya. Shapiro, and G. Quirion, Magnetic phases of the $S=5/2$ triangular-lattice antiferromagnet $\text{RbFe}(\text{MoO}_4)_2$ as determined by ultrasound velocity measurements, *Physical Review B* **103**, 224422 (2021).
- [85] Y. Kubota, H. Tanaka, T. Ono, Y. Narumi, and K. Kindo, Successive magnetic phase transitions in RuCl_3 : XY-like frustrated magnet on the honeycomb lattice, *Physical Review B* **91**, 094422 (2015).
- [86] D. L. Bergman, R. Shindou, G. A. Fiete, and L. Balents, Models of degeneracy breaking in pyrochlore antiferromagnets, *Physical Review B* **74**, 134409 (2006).
- [87] L. Capriotti, A. E. Trumper, and S. Sorella, Néel Order in the Triangular Heisenberg Model, *Physical Review Letters* **82**, 3899 (1999).
- [88] W. Zheng, J. O. Fjærestad, R. R. P. Singh, R. H. McKenzie, and R. Coldea, Excitation spectra of the spin- $\frac{1}{2}$ triangular-lattice Heisenberg antiferromagnet, *Physical Review B* **74**, 224420 (2006).
- [89] S. R. White and A. L. Chernyshev, Néel Order in Square and Triangular Lattice Heisenberg Models, *Physical Review Letters* **99**, 127004 (2007).
- [90] F. Mouhat and F.-X. Coudert, Necessary and sufficient elastic stability conditions in various crystal systems, *Physical Review B* **90**, 224104 (2014).
- [91] J. Villain, R. Bidaux, J.-P. Carton, and R. Conte, Order as an effect of disorder, *Journal de Physique* **41**, 1263 (1980).
- [92] M. T. Heinilä and A. S. Oja, Selection of the ground state in type-I fcc antiferromagnets in an external magnetic field, *Physical Review B* **48**, 7227 (1993).
- [93] M. E. Zhitomirsky, Real-space perturbation theory for frustrated magnets: Application to magnetization plateaus, *Journal of Physics: Conference Series* **592**, 012110 (2015).

Supplemental Material for “ \mathbb{Z}_2 Vortex Crystal Candidate in the Triangular $S = 1/2$ Quantum Antiferromagnet”

J. Nagl,^{1,*} K. Yu. Povarov,² B. Duncan,¹ C. Näppi,¹ D. Khalyavin,³ P. Manuel,³
 F. Orlandi,³ J. Sourd,² B. V. Schwarze,² F. Husstedt,² S. A. Zvyagin,² O. Zaharko,⁴
 P. Steffens,⁵ A. Hiess,^{5,6} D. Allan,⁷ S. Barnett,⁷ Z. Yan,¹ S. Gvasaliya,¹ and A. Zheludev^{1,†}

¹*Laboratory for Solid State Physics, ETH Zürich, 8093 Zürich, Switzerland*

²*Dresden High Magnetic Field Laboratory (HLD-EMFL) and Würzburg-Dresden Cluster of Excellence ct.qmat, Helmholtz-Zentrum Dresden-Rossendorf (HZDR), 01328 Dresden, Germany*

³*ISIS Facility, Rutherford Appleton Laboratory, Chilton, Didcot, Oxon OX11 0QX, United Kingdom*

⁴*PSI Center for Neutron and Muon Sciences, Forschungsstrasse 111, 5232 Villigen, PSI, Switzerland*

⁵*Institut Laue-Langevin, 71 avenue des Martyrs, CS 20156, 38042 Grenoble Cedex 9, France*

⁶*European Spallation Source ERIC, P.O. Box 176, 22100 Lund, Sweden*

⁷*Diamond Light Source, Harwell Science and Innovation Campus, Didcot, Oxfordshire OX11 0DE, UK*
 (Dated: December 2, 2025)

In this supplement, we provide supporting information about the low-temperature crystal structure, the single-ion fitting procedures & ESR data, the magnetoelastic coupling, our inelastic neutron spectroscopy experiment and the proposed magnetic structures.

I. CRYSTAL STRUCTURE & SPIN HAMILONIAN

(CD₃ND₃)₂NaRuCl₆ adopts a trigonal $P\bar{3}m1$ structure at room temperature [1], realizing an ideal triangular lattice of Ru³⁺ ions in the spin-orbital entangled $j_{\text{eff}} = 1/2$ state. The local point symmetry at the magnetic site amounts to $\bar{3}m$. In this case, the most general 2D spin Hamiltonian for nearest neighbors, including all anisotropy terms allowed by symmetry, contains *four* exchange parameters. In the global cartesian frame ($\hat{x} \parallel a$, $\hat{z} \parallel c$) it may be written as

$$\begin{aligned} \mathcal{H}_{\parallel} = & \sum_{\langle i,j \rangle} J(S_i^x S_j^x + S_i^y S_j^y + \Delta S_i^z S_j^z) \\ & + 2J_{\pm\pm}[(S_i^x S_j^x - S_i^y S_j^y) \cos(\varphi_{\alpha}) - (S_i^x S_j^y + S_i^y S_j^x) \sin(\varphi_{\alpha})] \\ & + J_{z\pm}[(S_i^y S_j^z + S_i^z S_j^y) \cos(\varphi_{\alpha}) - (S_i^x S_j^z + S_i^z S_j^x) \sin(\varphi_{\alpha})]. \end{aligned} \quad (1)$$

Here, the phases $\varphi_{\alpha} \in (0, 2\pi/3, 4\pi/3)$ associated with the primitive translation vectors $\mathbf{a}, \mathbf{b}, \mathbf{a} + \mathbf{b}$ give rise to a bond dependence on the anisotropic $J_{\pm\pm}, J_{z\pm}$ couplings. These triangular layers exhibit a direct AA-stacking, resulting in a simple inter-plane coupling restricted to XXZ form

$$\mathcal{H}_{\perp} = \sum_{\langle i,j \rangle} J_c(S_i^x S_j^x + S_i^y S_j^y + \Delta_c S_i^z S_j^z). \quad (2)$$

In both cases, a superexchange between next-nearest neighbors would involve significantly longer bond lengths (12.37 Å vs. 7.14 Å in the triangular plane, 9.86 Å vs. 6.80 Å between layers) and is unlikely to play an important role.

Towards lower temperatures, (CD₃ND₃)₂NaRuCl₆ goes through a structural transition. This is best seen in additional heat capacity measurements depicted in Fig. 1, carried out on a 4.5 mg single crystal sample in a 9 T Physical Property Measurement System (PPMS). The data show a clear lambda anomaly at $T^* \approx 118$ K, indicative of a continuous phase transition. An entropy release of order $\Delta S \sim R \log(2)$ would suggest a spontaneous choice between *two* structural configurations.

To characterize the structural changes near T^* , we performed high-resolution single crystal x-ray experiments at the I19 synchrotron beamline (Diamond, UK). Shelx-based refinement results on a representative sample are summarized in Tables I to III. A high-temperature dataset collected at 150 K ($T > T^*$) yields excellent agreement to a model based on the nominal $P\bar{3}m1$ crystal structure, with $R_1 = 1.3\%$ and less than 1 e/Å³ difference in electronic density. Due to their weak scattering, the light deuterium atoms are constrained with a riding model, assuming

* jnagl@ethz.ch

† zhelud@ethz.ch; <http://www.neutron.ethz.ch/>

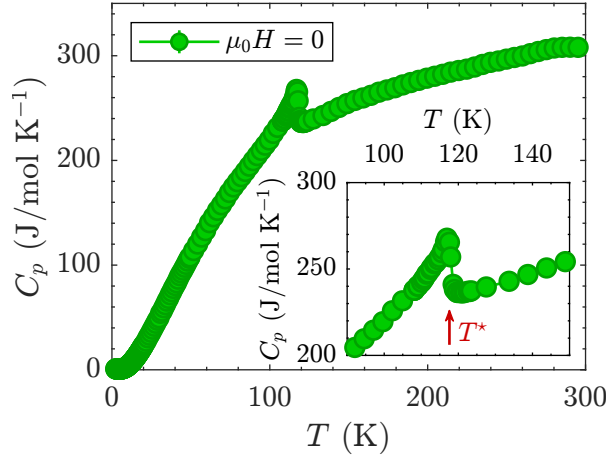


FIG. 1. Heat capacity in $(\text{CD}_3\text{ND}_3)_2\text{NaRuCl}_6$ against temperature, depicting a structural transition at T^* . The inset shows a zoom-in close to the lambda anomaly.

TABLE I. Summary of single crystal x-ray refinements of the chemical structure $(\text{CD}_3\text{ND}_3)_2\text{NaRuCl}_6$ at 150 K ($T > T^*$) and 30 K ($T < T^*$).

Characteristics	$T = 150$ K	$T = 30$ K, High Sym.	$T = 30$ K, Low Sym.
Chemical formula	$(\text{CD}_3\text{ND}_3)_2\text{NaRuCl}_6$	$(\text{CD}_3\text{ND}_3)_2\text{NaRuCl}_6$	$(\text{CD}_3\text{ND}_3)_2\text{NaRuCl}_6$
Wavelength (\AA)	0.689	0.689	0.689
Crystal System	Trigonal	Trigonal	Trigonal
Space Group	$P\bar{3}m1$	$P\bar{3}m1$	$P\bar{3}$
a, b (\AA)	7.1964(1)	7.1435(1)	7.1435(1)
c (\AA)	6.7939(1)	6.7984(1)	6.7984(1)
α, β (deg)	90	90	90
γ (deg)	120	120	120
V (\AA^3)	304.71(1)	300.44(1)	300.44(1)
Z	1	1	1
ρ_{calc} (g/cm^3)	2.25	2.28	2.28
$2\theta_{\text{max}}$ (deg)	116.74	116.74	116.74
Measured Reflections	37577	31016	31016
Independent Reflections	1750	1796	1796
Refined Parameters	18	18	23
R_1 (%)	1.33	9.68	2.45
wR_2 (%)	3.69	38.53	6.73
Goodness of Fit S	1.075	3.372	1.217
Twinning Ratio f	-	-	1.62 : 1
Diff. density ($\text{e}/\text{\AA}^3$)	0.65 / -0.91	15.35 / -13.45	2.11 / -3.27

an ideal CH_3 group with variable distance and thermal parameters fixed by the non-riding atom. Repeating an analogous refinement on a 30 K ($T < T^*$) dataset results in a significantly worse $R_1 = 9.68\%$, indicating some change in the chemical structure. None of the space groups consistent with the apparent Laue class $\bar{3}m1$ improve the fit.

This tension may be resolved by considering a transition into a low-symmetry $P\bar{3}$ structure. Such a model allows for 2-fold merohedral twinning, which can disguise the “true” Laue class and is consistent with the observed release of entropy. Here the mirror plane is lost, allowing the RuCl_6 octahedra and CD_3ND_3 molecules to rotate by $\pm\psi$ around the z -axis passing through the high-symmetry site ($1b$ and $2d$ respectively). Equivalently, this corresponds to a loss of 2-fold rotational symmetry around \mathbf{a} , \mathbf{b} or $\mathbf{a} + \mathbf{b}$. A possible twinning matrix would be $[-1 \ 0 \ 0; 1 \ 1 \ 0; 0 \ 0 \ 1]$. This model yields excellent agreement with the data, where $R_1 = 2.4\%$. Again, the deuterium positions are constrained by a riding model, though now the rotation angle of the CH_3 group also becomes a free parameter.

Final refinement results and structural differences between both models are visualized in Fig. 2 and Fig. 3. The rotation angle of the RuCl_6 octahedra at 30 K - controlling the degree of symmetry breaking - amounts to $\psi = \pm 2.95(1)^\circ$. Hints of the structural change are seen even in the high-symmetry $P\bar{3}m1$ model: The thermal parameters on chlorine are highly anisotropic, elongated in the triangular plane to cover both $\pm\psi$.

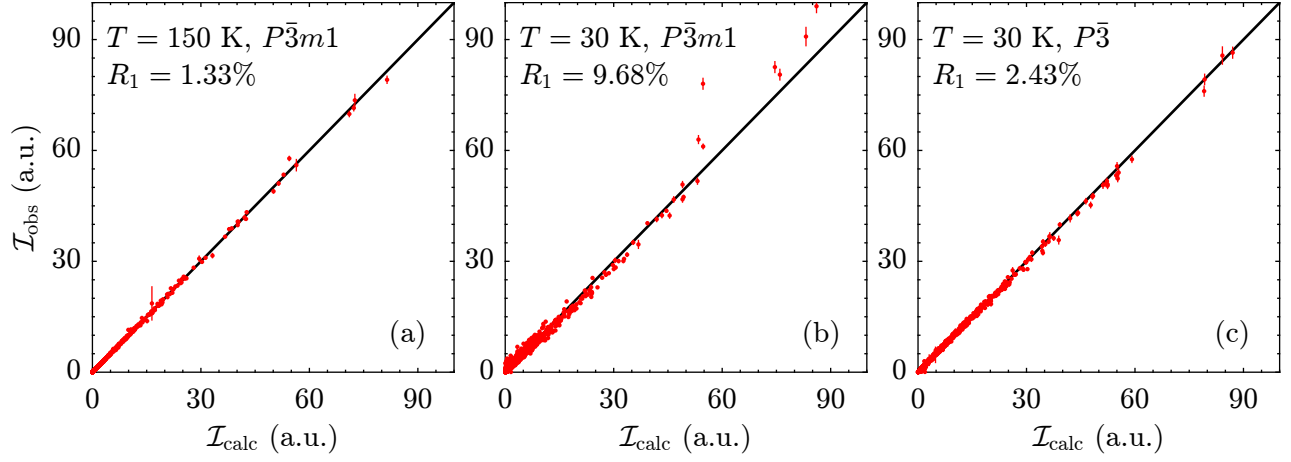


FIG. 2. Observed versus calculated x-ray intensities at 150 K in $P\bar{3}m1$ space group (a), at 30 K with the nominal $P\bar{3}m1$ structure (b) and at 30 K for a lower symmetry $P\bar{3}$ model including 2 merohedral twins. The solid line shows the 1:1 agreement in all panels.

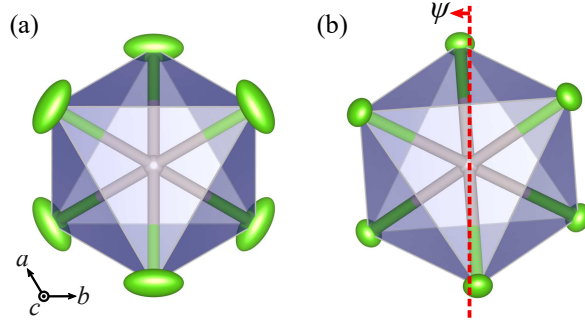


FIG. 3. RuCl_6 octahedra for single-crystal x-ray refinements at 30 K against different structural models. (a) Nominal $P\bar{3}m1$ structure and (b) lower-symmetry $P\bar{3}$ structure with parameters in tables I to III. The green ellipsoids illustrate the anisotropic thermal displacements, while the red line in (b) emphasizes the rotation of RuCl_6 octahedra by ψ .

We note that a non-centrosymmetric space group $P\bar{3}$ would also be consistent with the merohedral twinning scenario discussed above. However, our refinement attempts yield no improvement in R -factors despite the extra parameters. Analogous refinements were carried out on several single crystal samples, always pointing to the $P\bar{3}m1 \rightarrow P\bar{3}$ transition with analogous R -factors (8 – 10% vs. 1.5 – 2.5% for $P\bar{3}m1$ and $P\bar{3}$ models respectively). Similar structural changes have been reported in the triangular lattice systems $\text{RbFe}(\text{MoO}_4)_2$ [2] and $\text{Na}_2\text{BaCo}(\text{PO}_4)_2$ [3, 4], making this a relatively common structural motif.

Let's discuss the potential impact of this structural phase transition on the magnetism. Anti-symmetric Dzyaloshinskii-Moriya terms remain forbidden by symmetry, at least down to T_N (the same goes for anything akin to a $J - J'$ isosceles distortion). However, the lower point symmetry $\bar{3}$ at the Ru^{3+} site allows for two new symmetric anisotropy terms in the triangular lattice Hamiltonian of Eq. 1. We can parameterize these by adding separate phase shifts to the bond angles $\varphi_\alpha \rightarrow \varphi_\alpha + \delta\phi$, one for each of the bond-dependent terms $J_{\pm\pm}$ and $J_{z\pm}$.

As for the inter-plane coupling, the main effect of the transition would be to allow for two inequivalent diagonal terms $J_a \neq J_b$ [see Fig. 4(a)]. This has been explored previously in both $\text{RbFe}(\text{MoO}_4)_2$ [5, 6] and $\text{Na}_2\text{BaCo}(\text{PO}_4)_2$ [4]. The mean-field inter-plane exchange energy is given as

$$E(q_c) = -\frac{3}{2}JS^2 - \frac{1}{2}[3(J_a + J_b) - 2J_c]S^2 \cos(2\pi q_c) + \frac{3\sqrt{3}}{2}[J_b - J_a]S^2 \sin(2\pi q_c) \quad (3)$$

per site. In practice, any $J_a \neq J_b$ will entail an incommensurate (IC) *inter-plane* stacking $q_c \neq 1/2$, incompatible with experiment. We solve Eq. 3 numerically and plot the resulting inter-plane propagation vector in Fig. 4(b). By setting $q_c \equiv 1/2$ we can restrict $J_a \approx J_b < J_c/3$, so the main physics is captured purely by J_c .

TABLE II. Fractional atomic coordinates and thermal displacement parameters deduced from a refinement of single crystal x-ray diffraction data at $T = 150$ K against the nominal structural model with space group $P3m1$ (No. 164). The light deuterium atoms are constrained with a riding model (CH_3 group with variable distance).

Atom	Wyckoff	x	y	z	Equiv. B_{iso}
Na	1a	0	0	0	1.596(7)
Ru	1b	0	0	0.5	0.814(2)
Cl	6i	0.69054(2)	0.84527(2)	0.29605(2)	2.002(2)
N	2d	0.33333	0.66667	0.6592(1)	2.09(1)
C	2d	0.33333	0.66667	0.8741(2)	2.32(2)
D(1)	6i	0.26714	0.73811	0.61452	3.13
D(2)	6i	0.40828	0.59336	0.92220	3.48
B_{11}	B_{22}	B_{33}	B_{23}	B_{31}	B_{12}
1.95(1)	1.95(1)	0.89(1)	0	0	0.974(6)
0.875(2)	0.875(2)	0.692(2)	0	0	0.437(1)
1.077(2)	2.002(3)	1.123(3)	-0.114(1)	-0.227(2)	0.539(2)
2.487(2)	2.487(2)	1.287(2)	0	0	1.24(1)
2.835(2)	2.835(2)	1.303(2)	0	0	1.42(1)

TABLE III. Same as Table II, but for a refinement of the $T = 30$ K data against the reduced-symmetry space group $P\bar{3}$ (No. 147). Here the mirror plane is lost, allowing the Cl octahedra and CD_3ND_3 molecules to rotate. The light deuterium atoms are constrained with a riding model (CH_3 group with variable distance & rotation angle).

Atom	Wyckoff	x	y	z	Equiv. B_{iso}
Na	1a	0	0	0	0.70(1)
Ru	1b	0	0	0.5	0.345(2)
Cl	6g	0.68921(4)	0.82456(4)	0.29564(3)	0.575(3)
N	2d	0.33333	0.66667	0.3401(2)	0.86(1)
C	2d	0.33333	0.66667	0.1222(2)	0.99(2)
D(1)	6g	0.22734	0.69112	0.61527	1.26
D(2)	6g	0.44432	0.63561	0.92585	1.50
B_{11}	B_{22}	B_{33}	B_{23}	B_{31}	B_{12}
0.821(2)	0.821(2)	0.474(2)	0	0	0.411(9)
0.341(2)	0.341(2)	0.353(3)	0	0	0.166(2)
0.473(6)	0.644(7)	0.531(6)	-0.038(4)	-0.066(4)	0.220(5)
0.963(2)	0.963(2)	0.655(3)	0	0	0.48(1)
1.145(3)	1.145(3)	0.687(3)	0	0	0.57(2)

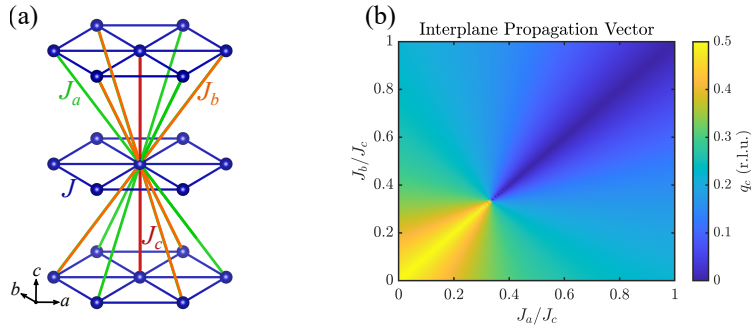


FIG. 4. Effects of structural transition on the inter-plane coupling. (a) The diagonal next-nearest neighbor interactions become inequivalent by symmetry, i.e. $J_a \neq J_b$. (b) Out-of-plane propagation vector component q_c obtained by minimizing the classical energy in Eq. 3. An $J_a \neq J_b$ should result in IC stacking along the c -axis.

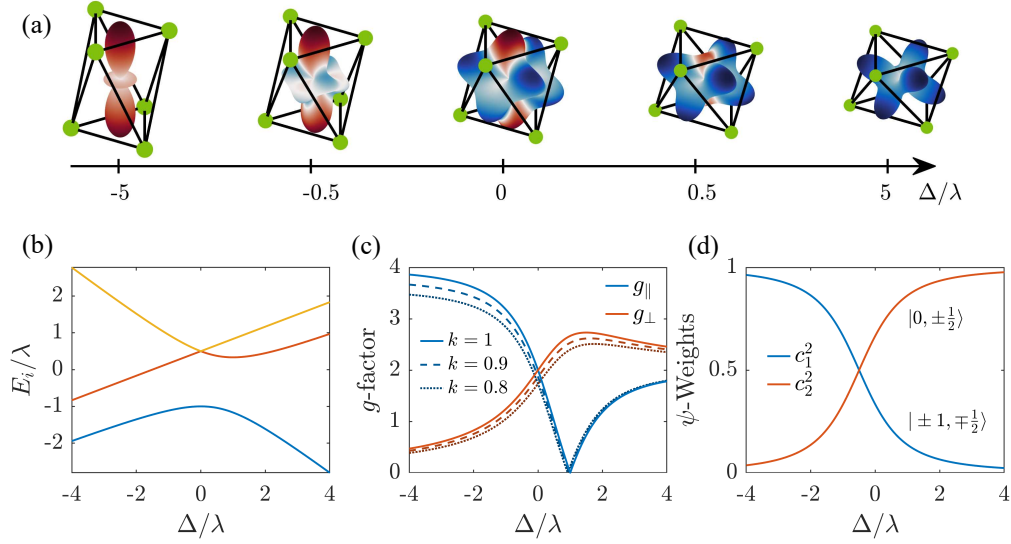


FIG. 5. Effects of trigonal distortion on the spin-orbital wavefunctions. (a) Sketch of the spatial shape of the pseudospin wavefunctions for different ratios Δ/λ . Red/blue color indicates spin up/down polarization of the hole. In (b,c,d) we show the dependence of the energy spectrum, g -factors and ground state weights on the trigonal distortion. Results of different k due to covalency effects are also depicted.

II. SINGLE-ION FITS & SPIN-ORBITAL WAVEFUNCTIONS

Here we summarize our fitting procedures of the single-ion + mean-field model discussed in the main text. We keep only the low-energy $\hat{\ell}_{\text{eff}} = 1$ (orbital) and $\hat{S} = 1/2$ (spin) degrees of freedom, corresponding to a single hole in the t_{2g} manifold. This results in the on-site Hamiltonian

$$\mathcal{H} = \lambda \hat{\ell} \cdot \hat{\mathbf{S}} + \Delta \hat{\ell}_z^2 - \mu_B \mathbf{H} \cdot \hat{\mathbf{M}} \quad (4)$$

where $\hat{\mathbf{M}} = 2\hat{\mathbf{S}} - k\hat{\ell}$ is the magnetization and $k \lesssim 1$ accounts for a small reduction in orbital moment due to hybridization with Cl^- anions (i.e. covalency effects [7, 8]). By diagonalizing \mathcal{H} , we obtain the energy spectrum E_i and eigenstates $|\psi_i\rangle$ (see Fig. 5). For dominant spin-orbit coupling $|\Delta/\lambda| \lesssim 1$, the ground state is a spin-orbital entangled $j_{\text{eff}} = 1/2$ Kramers doublet, written as

$$|\pm\rangle = c_1 |\pm 1, \mp 1/2\rangle + c_2 |0, \pm 1/2\rangle \quad (5)$$

where $c_{1,2} = \pm \sqrt{\frac{1}{2} \mp \frac{A}{2\sqrt{A^2+1}}}$ and $A = \frac{2\Delta/\lambda - 1}{2\sqrt{2}}.$

Larger trigonal distortions $|\Delta| \gg \lambda$ result in a more trivial state with no interesting orbital physics (the spin polarization of the hole is synonymous with that of the pseudospins, cf. red/blue colors in Fig. 5(a)), purely composed of $|\pm 1, \mp \frac{1}{2}\rangle$ or $|0, \pm \frac{1}{2}\rangle$ states (depending on the sign of Δ). In order to determine the Hamiltonian parameters, we use wavefunctions to calculate several experimentally accessible properties. The longitudinal/transverse g -factors are given as

$$g_{\parallel} = 2|(1+k)c_1^2 - c_2^2| \quad \text{and} \quad g_{\perp} = 2c_2(c_2 - \sqrt{2}kc_1). \quad (6)$$

The single-ion magnetization can be calculated as

$$M_{\alpha}^{\text{SI}}(\mathbf{H}, T) = \mu_B \sum_i p_i \langle \psi_i | 2\hat{S}_{\alpha} - k\hat{\ell}_{\alpha} | \psi_i \rangle, \quad (7)$$

where p_i are Boltzmann weights and the uniform susceptibility

$$\chi_{\alpha\beta} = \frac{\partial M_{\alpha}}{\partial H_{\beta}} \quad (8)$$

TABLE IV. Fit results of the single-ion + mean-field model against susceptibility, magnetization and ESR data.

Parameter	Value
λ	153.26 ± 0.03 meV
Δ	-77.94 ± 0.01 meV
k	0.9661 ± 0.0001
J_{MF}	1.71 ± 0.01 K
χ_a^0	$-9.2 \pm 4.8 \times 10^{-5}$ emu/mol
χ_c^0	$-6.5 \pm 1.2 \times 10^{-4}$ emu/mol

is simply evaluated numerically. For a direct comparison to experiment, we include also a temperature independent susceptibility contribution $\chi_{\alpha\beta}^0$ as well as a mean-field Heisenberg exchange parameter J_{MF} . Each ion experiences a local field \mathbf{H}_{MF} proportional to the magnetization of its neighbors, determined self-consistently using the relation

$$\mathbf{M}^{\text{MF}} = \mathbf{M}^{\text{SI}}(\mathbf{H} + \mathbf{H}_{\text{MF}}, T) \quad \text{where} \quad \mathbf{H}_{\text{MF}} = -\frac{zJ_{\text{MF}}}{(\mathbf{g}\mu_B)^2} \mathbf{M}^{\text{MF}}. \quad (9)$$

Here $z = 6$ is the number of nearest neighbors, while $\mathbf{g} = \text{diag}(g_{\perp}, g_{\perp}, g_{\parallel})$ is the g -tensor. By simultaneously fitting the magnetization, susceptibility and ESR data for all field directions we obtain the parameter estimates summarized in Table IV. We note that in experiment we are highly sensitive to the ratio Δ/λ , while the overall energy scale only appears in the high- T curvature of inverse susceptibilities and becomes muddled together with χ_{α}^0 . Therefore, one can still obtain reasonable agreement by changing both spin-orbit coupling and trigonal crystal field simultaneously within $\sim 20\%$, but $\Delta/\lambda \simeq -0.51$ remains tightly constrained.

III. ELECTRON SPIN RESONANCE

In Fig. 6 we present additional ESR data, characterizing the temperature dependence of the spectra discussed in the main text. For both $\mathbf{H} \parallel \mathbf{a}$ and $\mathbf{H} \parallel \mathbf{c}$ configurations, the resonance line is visible as a dip in optical transmission, which becomes broader and more intense upon cooling. In both cases the Larmor frequency, i.e. the g -factor, does not seem to change with temperature.

IV. MAGNETOELASTICS & EXCHANGE STRICTION

Let us recall the exchange striction mechanism commonly responsible for magnetoelastic effects near phase transitions in magnetic insulators [9]. Exchange integrals critically depend on the distances between magnetic ions, as well as their angles with the ligands mediating the bonding. For small changes, this can be linearized as

$$J(|\mathbf{r}_i - \mathbf{r}_j|) = J(|\mathbf{r}_{ij}^0|) + \rho_{ij} \frac{\partial J}{\partial \rho_{ij}} \bigg|_{\rho_{ij}=0} + \mathcal{O}(\rho_{ij}^2) \quad (10)$$

where $\rho_{ij} = |\delta \mathbf{r}_{ij}|/|\mathbf{r}_{ij}^0|$ is a normalized bond displacement induced by some lattice strain ε_{Γ} . This allows us to write down a simple “bond-phonon” [10, 11] magnetoelastic Hamiltonian

$$\mathcal{H}_{\text{m-e}} = \sum_{\langle i,j \rangle} \left[(J_0 - g\rho_{ij}) \mathbf{S}_i \cdot \mathbf{S}_j + \frac{k}{2} \rho_{ij}^2 \right] \quad (11)$$

where k is an elastic modulus and the coupling constant $g \equiv -\frac{\partial J}{\partial \rho_{ij}}$ sets the strength of spin-lattice effects. In equilibrium we have $\partial \mathcal{H} / \partial \rho_{ij} = 0$, which yields $\langle \rho_{ij} \rangle = \frac{g}{k} \langle \mathbf{S}_i \cdot \mathbf{S}_j \rangle$ for the normalized changes in bond length. As spin correlations develop below T_N , each bond acquires an additional stiffness contribution $\propto \langle \mathbf{S}_i \cdot \mathbf{S}_j \rangle$ and the lattice contracts to accommodate this. In principle one can “integrate out” the phonon terms in the Hamiltonian, which produces an effective bi-quadratic term $\sim b(\mathbf{S}_i \cdot \mathbf{S}_j)^2$ in the spin model where $b_{\text{eff}} = -g^2/k$.

A. Estimating the Coupling Constants

Based on the lattice strains $\Delta l/l$ determined in zero field, we attempt to estimate the magnetoelastic coupling constants. To check which type of distortions may be realized, we look at the symmetry strains, irreps of the

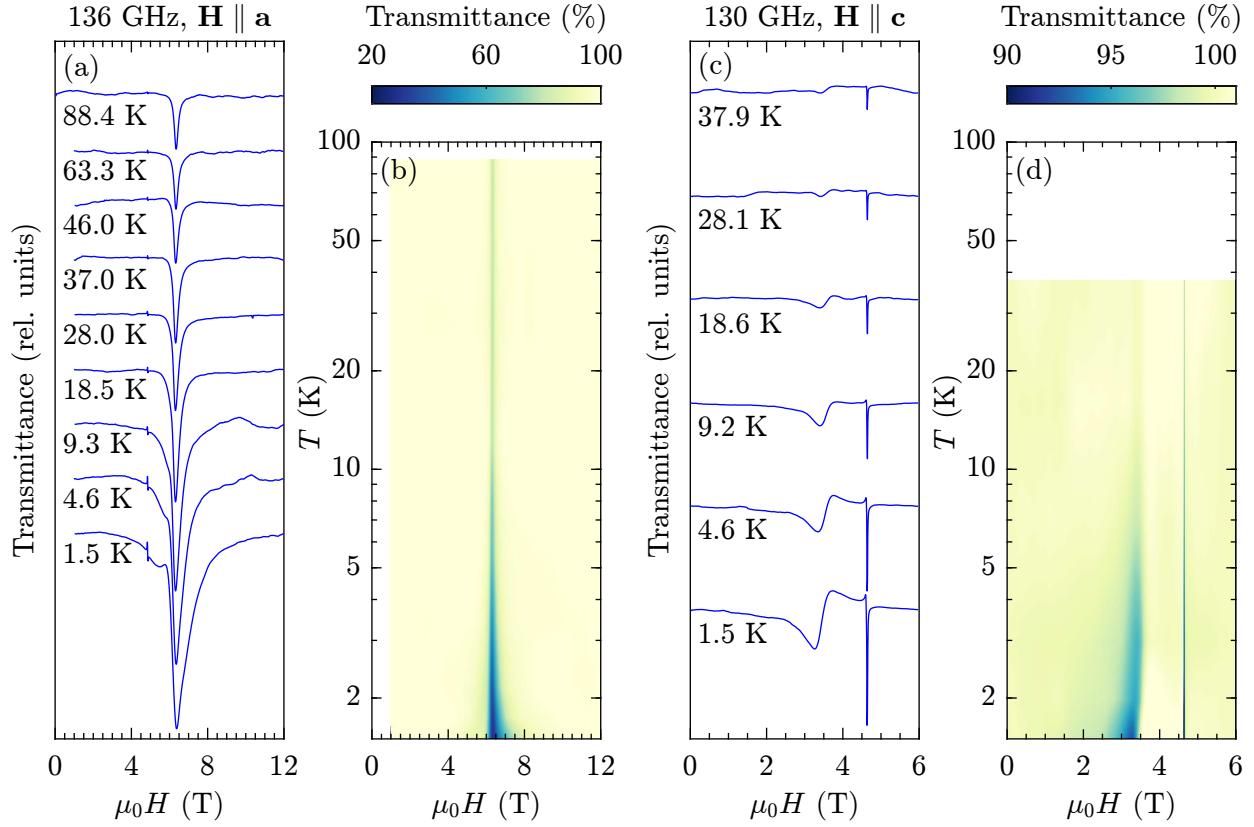


FIG. 6. Temperature dependence of electron spin resonance excitations. (a,c) Fixed frequency ESR spectra at various temperatures in $\mathbf{H} \parallel \mathbf{a}$ and $\mathbf{H} \parallel \mathbf{c}$ experimental configurations. (b,d) False colorplots of the optical transmittance against temperature and magnetic field.

Mode	δr_{12}	δr_{13}	δr_{23}
A_1	-1	-1	-1
$E(1)$	1	$-\frac{1}{2}$	$-\frac{1}{2}$
$E(2)$	0	$\frac{\sqrt{3}}{2}$	$-\frac{\sqrt{3}}{2}$

TABLE V. Bond elongation δr_{ij} for D_3 symmetry strains (i.e. vibrational modes) A_1 and E of an equilateral triangle.

fundamental vibrational modes that may deform the crystal [12]. Restricting ourselves to the case of $\mathbf{k} = 0$ distortions, the problem simplifies to that of the D_3 point group for an equilateral triangle. There are two relevant irreps: The trivial A_1 “breathing” mode, expanding/contracting the entire triangle, and a two-fold degenerate E mode allowing e.g. for a $J - J'$ isosceles distortion.

The simple A_1 mode should be always active, since the magnetic energy depends linearly on the strain ε_{A_1} , e.g.

$$E_{\text{mag}}(\varepsilon) \approx -\frac{3}{2}(J - g_{A_1} \langle \varepsilon_{A_1} \rangle) S^2 + \mathcal{O}(\varepsilon^2) \quad (12)$$

for a classical Heisenberg model on the triangular lattice. As for the “real” low-temperature structure, we take $\langle \mathbf{S}_i \cdot \mathbf{S}_j \rangle \approx -\frac{1}{2} \langle S \rangle^2$ with a reduced ordered moment $\langle S \rangle \approx 0.21$ [13–15] and ignore the small incommensurability (the angles between adjacent spins remain close to 120°). The relevant stiffness constant is $k = \frac{V_0(c_{11}+c_{12})}{2}$, where V_0 is the unit cell volume, the longitudinal sound velocity $v_{11} = \sqrt{c_{11}/\rho} \simeq 2.1$ km/s is determined from ultrasound and ρ represents the mass density. Here we make the rough assumption $k \sim \frac{3V_0 c_{11}}{4}$ based on the elastic stability conditions $0 < c_{12} < c_{11}$ for hexagonal crystals [16]. Given the strain $\langle \varepsilon_{A_1} \rangle \equiv \Delta l/l \sim -5 \times 10^{-6}$ observed in our zero field thermal expansion data, we estimate the spin-lattice coupling constant

$$g_{A_1} = \frac{k \Delta l/l}{\langle \mathbf{S}_i \cdot \mathbf{S}_j \rangle} \sim 40 \text{ K}. \quad (13)$$

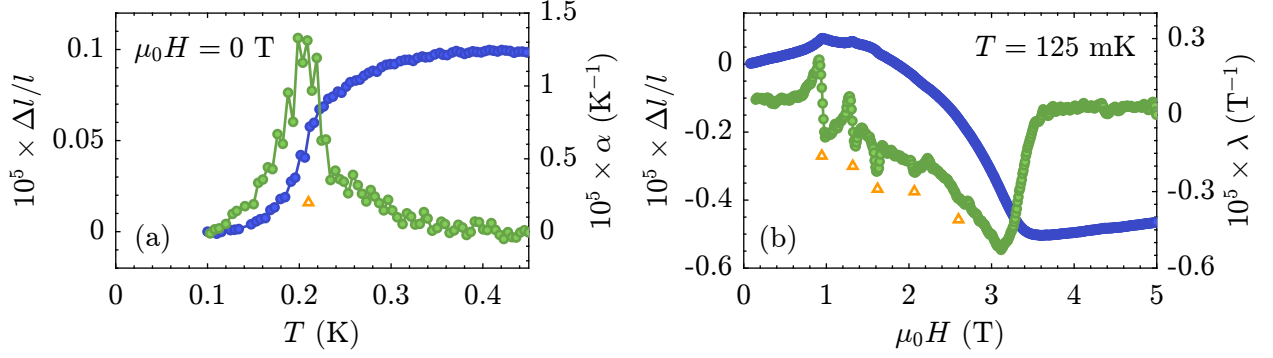


FIG. 7. Magnetoelastic effects in $(\text{CD}_3\text{ND}_3)_2\text{NaRuCl}_6$ perpendicular to the triangular planes. (a) Temperature dependent sample dilation $\Delta l/l$ along the c -axis, together with its numerical derivative, the thermal expansion coefficient $\alpha = \frac{1}{l} \frac{\partial \Delta l}{\partial T}$. (b) Changes in sample length in a magnetic field $\mathbf{H} \parallel \mathbf{c}$, along with the magnetostriction coefficient $\lambda = \frac{1}{\mu_0 l} \frac{\partial \Delta l}{\partial H}$. Orange triangles in both panels denote the anomalies in $\alpha(T)$ and $\lambda(H)$, in agreement with the phase transitions discussed in the main text.

B. $J - J'$ Magnetoelastic Distortion

While our x-ray data confirm the trigonal crystal structure down to T_N , they cannot rule out the possibility of a “dynamic” $J - J'$ isosceles distortion coupled to the magnetic order parameter. Such a monoclinic lattice distortion would correspond to the $E(1)$ vibrational mode and may coexist with A_1 below T_{N2} on a similar scale $\lesssim 10^{-6}$. Starting from a simple Heisenberg picture, the triangular lattice would be deformed into inequivalent “chain” and “zig-zag” couplings with renormalized exchanges $J_0 \rightarrow J = J_0(1 - \epsilon)$ and $J_0 \rightarrow J' = J_0(1 + \frac{\epsilon}{2})$ respectively (here we define $\epsilon \equiv g_{E_1} \langle \langle \varepsilon_{E(1)} \rangle \rangle / J_0$ in the above exchange-striction framework). This affects both the classical propagation vector and the ground state energy, resulting in

$$|\mathbf{q}(\epsilon)| = 2 \cos^{-1} \left(-\frac{J'}{2J} \right) = 2 \cos^{-1} \left(-\frac{1 + \epsilon/2}{2(1 - \epsilon)} \right) = \frac{4\pi}{3} + \sqrt{3}\epsilon + \mathcal{O}(\epsilon^2) \quad (14)$$

$$E_{\text{mag}}(\epsilon) = J \cos(q) + 2J' \cos\left(\frac{q}{2}\right) = -\frac{3}{2}J_0 S^2 - \frac{9}{8}J_0 S^2 \epsilon^2 + \mathcal{O}(\epsilon^3). \quad (15)$$

Qualitatively, this approach can explain the IC peak positions observed in zero field as due to three structural domains with an underlying spiral ground state. However, there are several problems with such a theory. First off, a lattice distortion $\langle \langle \varepsilon_{E(1)} \rangle \rangle \sim 10^{-6}$ consistent with experiment would require a *huge* coupling constant $g_{E(1)} \sim 10^3 g_{A_1}$ to explain the IC shift $\delta q/q = 3\sqrt{3}g_{E(1)} \langle \langle \varepsilon_{E(1)} \rangle \rangle / 4\pi J_0 \sim 2\%$ of magnetic Bragg peaks observed experimentally. This in turn would necessitate a stiffness constant $k_{E(1)} = \frac{v(c_{11} - c_{12})}{2}$ three orders of magnitude smaller, i.e. $c_{11} - c_{12} \sim 10^{-3} c_{11}$. What’s even more problematic is that the classical magnetic energy gain from the distortion is *quadratic* in the strain at lowest order, not linear. The latter is directly competing against the cost in elastic energy (also quadratic), which means an E-type distortion is generally not expected to appear.

C. Dilatometry in $\mathbf{E} \parallel \mathbf{c}$ Geometry

In Fig. 7 we present additional dilatometry data in the $\mathbf{H} \parallel \mathbf{E} \parallel \mathbf{c}$ configuration, showing the length changes *perpendicular* to the triangular planes. We observe the same phase transitions discussed in the main text, both against temoerature (thermal expansion) and magnetic field (magnetostriction). Note that the overall scale of these magnetoelastic effects is roughly an order of magnitude weaker than within the triangular plane, as expected for a quasi-2D system.

V. INELASTIC NEUTRON SCATTERING

In the following, we provide further details about the sample and fitting procedure employed for the neutron spectroscopy experiment carried out at THALES (ILL). Fig. 8(a) shows a picture of the coaligned probe, composed of 16 crystals fixed to a copper holder with cytop glue and teflon. The total sample mass amounts to $m = 1.9$ g. The quality of the alignment can be seen in Fig. 8(b,c), with a sample mosaic of roughly 3° FWHM. One can also spot a

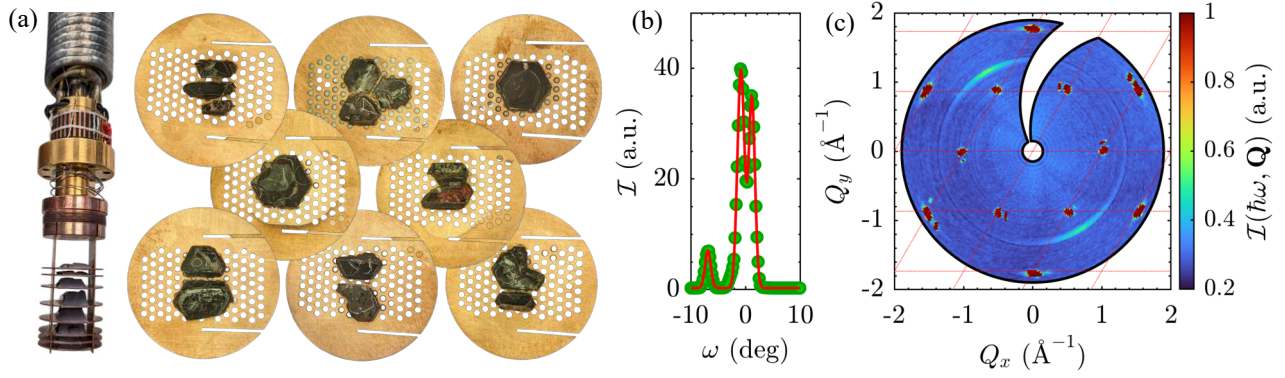


FIG. 8. (a) The probe used for neutron spectroscopy, containing 16 single crystals coaligned in the ab scattering plane. (b) A cut through the $\mathbf{Q} = (1, 0, 0)$ nuclear Bragg peak. (c) Elastic neutron scattering intensity in the $(hk0)$ plane taken at $T \simeq 1$ K. The powder line visible at $|\mathbf{Q}| \sim 1.3 \text{ \AA}^{-1}$ originates from teflon.

small crystallite, slightly misaligned by 6.9° in the $(hk0)$ plane and contributing about 7(2)% to the total scattering intensity.

To reconstruct the spin-wave dispersion relation presented in the main text, we masked out spurious intensity from inelastically re-scattered Bragg peaks (“Currat-Axe spurions”), subtracted a constant background and normalized the data by the magnetic form factor. We then averaged over the various equivalent reciprocal space paths presented in Fig. 9(a-c) and performed Gaussian fits to constant- \mathbf{Q} cuts in order to extract the dispersion points $\hbar\omega_{\mathbf{Q}}$.

These observations are compared to the magnon dispersion of a fully polarized ferromagnetic state in a least squared fitting procedure. There is only one branch (propagation vector $\mathbf{q} = \Gamma$) and spin-wave theory is exact [17], making this the perfect regime to extract exchange parameters. For longitudinal fields $\mathbf{H} \parallel \mathbf{c}$, the magnon dispersion for the general anisotropic spin Hamiltonian of Eq. 1 is given as

$$\begin{aligned} \hbar\omega(\mathbf{Q}) &= 2S\sqrt{A_{\mathbf{Q}}^2 - |B_{\mathbf{Q}}|^2} \\ A_{\mathbf{Q}} &= g_c\mu_B B_z - 3J\Delta + J\gamma_1(\mathbf{Q}) \\ B_{\mathbf{Q}} &= J_{\pm\pm} \left(\gamma_2(\mathbf{Q}) + \sqrt{3}i[\cos(2\pi k) - \cos(2\pi(h+k))] \right), \end{aligned} \quad (16)$$

where

$$\begin{aligned} \gamma_1(\mathbf{Q}) &= \cos(2\pi h) + \cos(2\pi k) + \cos(2\pi(h+k)) \\ \gamma_2(\mathbf{Q}) &= -2\cos(2\pi h) + \cos(2\pi k) + \cos(2\pi(h+k)). \end{aligned} \quad (17)$$

In this geometry, $J_{z\pm}$ is absent entirely from the spin-wave dispersion. Furthermore, at high fields we have $|A_{\mathbf{Q}}| \gg |B_{\mathbf{Q}}|$, i.e. $\hbar\omega(\mathbf{Q}) \approx 2S|A_{\mathbf{Q}}|$ and we are mainly sensitive to the XXZ-type couplings with only a weak dependence on $|J_{\pm\pm}|$. In the Heisenberg limit ($\Delta = 1, J_{\pm\pm} = J_{z\pm} = 0$), Eq. 16 simplifies to

$$\hbar\omega(\mathbf{Q}) = 2S(g_c\mu_B B_z - 3J + J\gamma_1(\mathbf{Q})). \quad (18)$$

The χ^2 goodness-of-fit metrics, obtained by fitting the experimental dispersion relation to the Heisenberg and the anisotropic model, are depicted in Fig. 9(d-g).

VI. COMMENSURATE MAGNETIC STRUCTURES

Here we discuss the nature of the commensurate magnetic structures in $(\text{CD}_3\text{ND}_3)_2\text{NaRuCl}_6$. Their essential physics can be understood through a Heisenberg model on the triangular lattice, with the addition of a small AFM inter-plane coupling $J_c > 0$ [18]. Given the observed propagation vector $\mathbf{q} = (1/3, 1/3, 1/2)$, we find the ground state by considering all possible six-sublattice spin configurations and resorting to semi-classical energy minimization. At $T = 0$, the classical degeneracy is lifted only by quantum fluctuations (i.e. order-by-disorder selection), favoring the “most collinear” states with the softest excitation spectrum [19, 20]. On a phenomenological level, one can emulate this by adding a small bi-quadratic coupling $\sim b(\mathbf{S}_i \cdot \mathbf{S}_j)^2$ to the Hamiltonian [21–23]. In fact, such a term can be derived rigorously through real space perturbation theory (RSPT), by calculating the leading order corrections to the

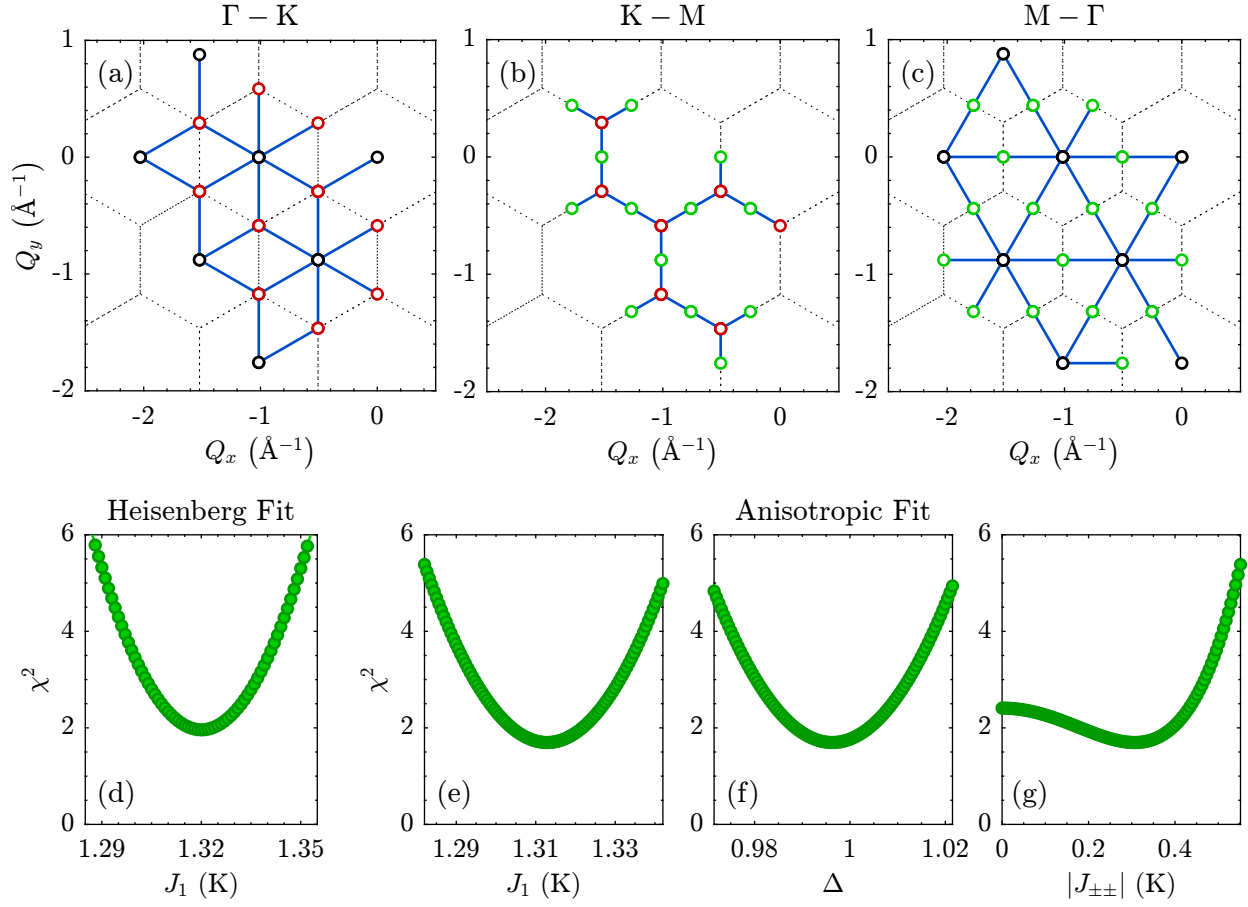


FIG. 9. (a-c) Schematic showing the equivalent reciprocal space paths along $\Gamma - K$, $K - M$ and $M - \Gamma$, used to plot the averaged excitation spectrum in the main text. Brillouin zone boundaries are indicated as black dotted lines. (d) χ^2 goodness-of-fit metric of the extracted dispersion relation to a nearest-neighbor Heisenberg model on the 2D triangular lattice. (e-g) Analogous χ^2 plots for the general anisotropic spin model of Eq. 1.

“mean field” (i.e. classical) ground state energy. For the triangular lattice Heisenberg antiferromagnet, the second order RSPT correction is given as [24]

$$\delta E_2 = \sum_n \frac{\langle 0 | \hat{V} | n \rangle \langle n | \hat{V} | 0 \rangle}{E_0 - E_n} = - \frac{J^2 S^2}{8H_{\text{loc}}} \sum_{\langle i,j \rangle} (1 - \cos \theta_{ij})^2 \quad (19)$$

where $H_{\text{loc}} = 3JS$ is the local field acting on each spin, resulting in $b_{\text{eff}} \equiv -J/(24S^3)$. Since this energy correction amounts to an effective Hamiltonian operating on the ground state manifold of classical vector spins $\mathbf{n}_i = \mathbf{S}_i/S$, the bi-quadratic term $\sim \cos^2 \theta_{ij} = (\mathbf{n}_i \cdot \mathbf{n}_j)^2$ can show up even for $S = 1/2$ quantum systems.

We find the optimal six-sublattice ground state by minimize the following semi-classical Hamiltonian

$$\mathcal{H} = \sum_{\langle i,j \rangle \in \Delta} [J\mathbf{S}_i \cdot \mathbf{S}_j + b_{\text{eff}}(S^2 - \mathbf{S}_i \cdot \mathbf{S}_j)^2] + J_c \sum_{\langle i,j \rangle \parallel c} \mathbf{S}_i \cdot \mathbf{S}_j - \sum_i \mathbf{S}_i \cdot \mathbf{H} \quad (20)$$

as a function of the inter-plane coupling J_c and magnetic field H , resulting in the spin configurations discussed in the main text. The phase diagram, as well as magnetization curves for a reasonable parameter choice $J_c = 0.1J$, are shown in Fig. 10. There are two differences compared to the pure 2D model: Firstly, the inter-plane term becomes frustrated by the field, resulting in a mixed FM-AFM stacking with both $\mathbf{q} = (1/3, 1/3, 1/2)$ and $2\mathbf{q} = (1/3, 1/3, 0)$ Fourier components. Furthermore, the stacking preferred just above the plateau differs from the one close to saturation, which gives rise to a first-order transition around $H_c \approx 0.7H_{\text{sat}}$, above/below which the choice of minority spin is uniform/staggered between layers. The evolution between phases Y - $\uparrow\uparrow\downarrow$ - V - V' appears to be highly robust with respect to J_c , until the collinear magnetization plateau eventually becomes suppressed for large $J_c \gtrsim 0.5J$.

Finally, we remark on the effects of other perturbing terms on these magnetic structures. The presence of several IC phases in $(\text{CD}_3\text{ND}_3)_2\text{NaRuCl}_6$ clearly points to significant bond-dependent interactions or magnetoelastic effects.

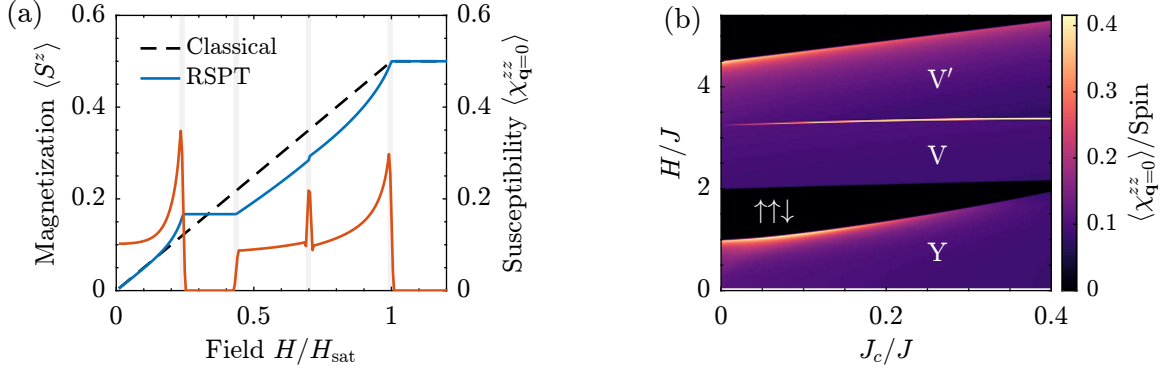


FIG. 10. Effects of inter-plane coupling on the magnetic structures for the Heisenberg triangular lattice antiferromagnet. (a) Magnetization curve and its numerical derivative for $J_c = 0.1J$, obtained from semi-classical model discussed in the text. (b) $T = 0$ ground state phase diagram in the same approach, visualized as false color plot of the uniform magnetic susceptibility $\chi(J_c, H)$. Both panels clearly show the presence of an additional phase transition between the V and V' states.

But towards the center of the phase diagram, the energy gain through order-by-disorder is maximized, surpassing those other contributions and leading to a lock-in to the semi-classical commensurate states discussed above [22, 25]. In absence of a lattice distortion, magnetoelastic effects can only contribute a tiny bi-quadratic term (~ 20 times smaller than the one obtained from RSPT, see Sec. IV) and should be irrelevant. The bond anisotropies would favor collinear four-sublattice stripe order [26]. Below some critical exchange ratio, their main effect would be to renormalize the critical fields H_c and break the $U(1)$ rotational symmetry, pinning the staggered in-plane ordered moment to some discrete orientation.

VII. \mathbb{Z}_2 VORTEX CRYSTAL PHASE

For sake of completeness, we reproduce here the expected 2D spin configuration for the \mathbb{Z}_2 vortex crystal phase [27–29]. Taking the cubic axes, one can equivalently re-write the spin Hamiltonian of Eq. 1 as a $J_0 - K - \Gamma - \Gamma'$ model [26]. The vortex crystal has been predicted to exist in the Heisenberg-Kitaev limit (i.e. $\Gamma = \Gamma' = 0$), where

$$\mathcal{H} = J_0 \sum_{\langle i,j \rangle} \mathbf{S}_i \cdot \mathbf{S}_j + K \sum_{\gamma \parallel \langle i,j \rangle} S_i^\gamma S_j^\gamma \quad (21)$$

and the coordinate transformation amounts to $J_0 = J + 6J_{\pm\pm}$, $K = -6J_{\pm\pm}$ with the constraints $\Delta = 1$ (confirmed experimentally in $(\text{CD}_3\text{ND}_3)_2\text{NaRuCl}_6$) and $J_{z\pm} = 2\sqrt{2}J_{\pm\pm}$ (yet to be determined). In momentum space, the classical HK-Hamiltonian has three eigenvalues at

$$\mathcal{J}^{\gamma\gamma}(\mathbf{q}) = K \cos(\mathbf{q} \cdot \hat{\mathbf{e}}_\gamma) + J \sum_{\alpha=x,y,z} \cos(\mathbf{q} \cdot \hat{\mathbf{e}}_\alpha), \quad (22)$$

i.e. each spin component $\gamma \in (x, y, z)$ prefers a different ordering vector. We obtain three sets of incommensurate positions $\pm \mathbf{q}^\gamma$, along the Γ -K direction in momentum space. These minima move towards the Γ (M)-point for positive (negative) K , where

$$|\mathbf{q}| = 1 - \frac{1}{\pi} \cos^{-1} \left(\frac{J}{2(J+K)} \right) \implies |\delta \mathbf{q}| \approx \frac{1}{\sqrt{3}\pi} \frac{|K|}{|J + \frac{7}{6}K|}. \quad (23)$$

A simple superposition of three such incommensurate spirals will not be a good ground state - the moment size would be strongly modulated. Instead the system would turn anharmonic, introducing additional Fourier components to retain a semi-classical equal moment structure. The resulting ground state preserves threefold symmetry and locally mimics the “parent” 120° structure, but exhibits a superlattice of \mathbb{Z}_2 vortices on larger length scales. Up to second harmonics, the magnetic structure may be approximated as

$$\mathbf{S}^\gamma(\mathbf{r}) = \frac{4S}{3\sqrt{3}} \text{Re} \left[e^{i[\mathbf{q}_\gamma \cdot \mathbf{r} + \phi]} + \frac{1}{4} \sum_{\alpha \neq \gamma} e^{i[(\mathbf{q}_\gamma + \mathbf{q}_\alpha) \cdot \mathbf{r} + \phi]} \right] \quad (24)$$

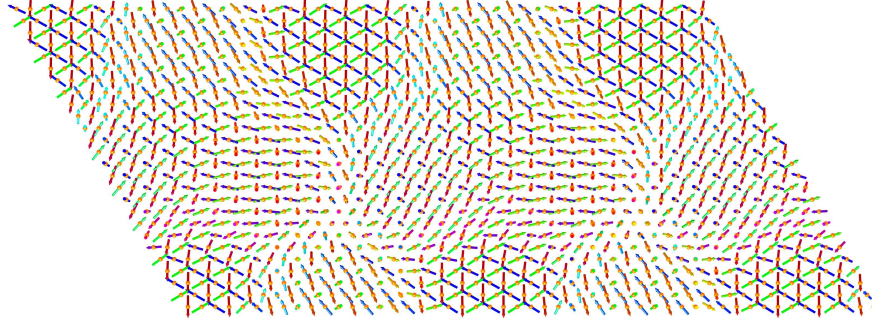


FIG. 11. Sketch of the 2D spin configuration for a \mathbb{Z}_2 vortex crystal in the Heisenberg-Kitaev model, with parameters $K/J_0 = -0.3$. The *hsv*-color of each spin indicates its rotation angle in the triangular plane.

with a phase shift $\phi = 2\pi n/3$ between sublattices, visualized in Fig. 11.

-
- [1] P. Vishnoi, J. L. Zuo, T. A. Strom, G. Wu, S. D. Wilson, R. Seshadri, and A. K. Cheetham, Structural Diversity and Magnetic Properties of Hybrid Ruthenium Halide Perovskites and Related Compounds, *Angewandte Chemie International Edition* **59**, 8974 (2020).
 - [2] A. Wařkowska, L. Gerward, J. Staun Olsen, W. Morgenroth, M. Maćzka, and K. Hermanowicz, Temperature- and pressure-dependent lattice behaviour of $\text{RbFe}(\text{MoO}_4)_2$, *Journal of Physics: Condensed Matter* **22**, 055406 (2010).
 - [3] Y. Kajita, T. Nagai, S. Yamagishi, K. Kimura, M. Hagihala, and T. Kimura, Ferroaxial Transitions in Glaserite-Type $\text{Na}_2\text{BaM}(\text{PO}_4)_2$ ($\text{M} = \text{Mg}, \text{Mn}, \text{Co}$, and Ni), *Chemistry of Materials* **36**, 7451 (2024).
 - [4] L. Woodland, R. Okuma, J. R. Stewart, C. Balz, and R. Coldea, From continuum excitations to sharp magnons via transverse magnetic field in the spin- $\frac{1}{2}$ ising-like triangular lattice antiferromagnet $\text{Na}_2\text{BaCo}(\text{PO}_4)_2$, *Phys. Rev. B* **112**, 104413 (2025).
 - [5] A. J. Hearmon, F. Fabrizi, L. C. Chapon, R. D. Johnson, D. Prabhakaran, S. V. Streltsov, P. J. Brown, and P. G. Radaelli, Electric Field Control of the Magnetic Chiralities in Ferroaxial Multiferroic $\text{RbFe}(\text{MoO}_4)_2$, *Physical Review Letters* **108**, 237201 (2012).
 - [6] A. Zelenskiy, J. A. Quilliam, A. Ya. Shapiro, and G. Quirion, Magnetic phases of the $S=5/2$ triangular-lattice antiferromagnet $\text{RbFe}(\text{MoO}_4)_2$ as determined by ultrasound velocity measurements, *Physical Review B* **103**, 224422 (2021).
 - [7] A. Abragam and B. Bleaney, *Electron Paramagnetic Resonance of Transition Ions*, 1st ed., Oxford classic texts in the physical sciences (Oxford University Press, 1970).
 - [8] Y. Kubota, H. Tanaka, T. Ono, Y. Narumi, and K. Kindo, Successive magnetic phase transitions in RuCl_3 : XY-like frustrated magnet on the honeycomb lattice, *Physical Review B* **91**, 094422 (2015).
 - [9] M. E. Lines, Elastic properties of magnetic materials, *Physics Reports* **55**, 133 (1979).
 - [10] K. Penc, N. Shannon, and H. Shiba, Half-Magnetization Plateau Stabilized by Structural Distortion in the Antiferromagnetic Heisenberg Model on a Pyrochlore Lattice, *Physical Review Letters* **93**, 197203 (2004).
 - [11] D. L. Bergman, R. Shindou, G. A. Fiete, and L. Balents, Models of degeneracy breaking in pyrochlore antiferromagnets, *Physical Review B* **74**, 134409 (2006).
 - [12] O. Tchernyshyov, R. Moessner, and S. L. Sondhi, Order by Distortion and String Modes in Pyrochlore Antiferromagnets, *Physical Review Letters* **88**, 067203 (2002).
 - [13] L. Capriotti, A. E. Trumper, and S. Sorella, Néel Order in the Triangular Heisenberg Model, *Physical Review Letters* **82**, 3899 (1999).
 - [14] W. Zheng, J. O. Fjærestad, R. R. P. Singh, R. H. McKenzie, and R. Coldea, Excitation spectra of the spin- $\frac{1}{2}$ triangular-lattice Heisenberg antiferromagnet, *Physical Review B* **74**, 224420 (2006).
 - [15] S. R. White and A. L. Chernyshev, Néel Order in Square and Triangular Lattice Heisenberg Models, *Physical Review Letters* **99**, 127004 (2007).
 - [16] F. Mouhat and F.-X. Coudert, Necessary and sufficient elastic stability conditions in various crystal systems, *Physical Review B* **90**, 224104 (2014).
 - [17] R. Coldea, D. A. Tennant, K. Habicht, P. Smeibidl, C. Wolters, and Z. Tylczynski, Direct Measurement of the Spin Hamiltonian and Observation of Condensation of Magnons in the 2D Frustrated Quantum Magnet Cs_2CuCl_4 , *Physical Review Letters* **88**, 4 (2002).
 - [18] D. Yamamoto, G. Marmorini, and I. Danshita, Microscopic Model Calculations for the Magnetization Process of Layered Triangular-Lattice Quantum Antiferromagnets, *Physical Review Letters* **114**, 027201 (2015).
 - [19] J. Villain, R. Bidaux, J.-P. Carton, and R. Conte, Order as an effect of disorder, *Journal de Physique* **41**, 1263 (1980).
 - [20] A. V. Chubukov and D. I. Golosov, Quantum theory of an antiferromagnet on a triangular lattice in a magnetic field, *Journal of Physics: Condensed Matter* **3**, 69 (1991).

- [21] M. T. Heinilä and A. S. Oja, Selection of the ground state in type-I fcc antiferromagnets in an external magnetic field, [Physical Review B **48**, 7227 \(1993\)](#).
- [22] C. Griset, S. Head, J. Alicea, and O. A. Starykh, Deformed triangular lattice antiferromagnets in a magnetic field: Role of spatial anisotropy and Dzyaloshinskii-Moriya interactions, [Physical Review B **84**, 245108 \(2011\)](#).
- [23] G. Koutroulakis, T. Zhou, Y. Kamiya, J. D. Thompson, H. D. Zhou, C. D. Batista, and S. E. Brown, Quantum phase diagram of the $S = \frac{1}{2}$ triangular-lattice antiferromagnet $\text{Ba}_3\text{CoSb}_2\text{O}_9$, [Physical Review B **91**, 024410 \(2015\)](#).
- [24] M. E. Zhitomirsky, Real-space perturbation theory for frustrated magnets: Application to magnetization plateaus, [Journal of Physics: Conference Series **592**, 012110 \(2015\)](#).
- [25] R. Chen, H. Ju, H.-C. Jiang, O. A. Starykh, and L. Balents, Ground states of spin-1/2 triangular antiferromagnets in a magnetic field, [Physical Review B **87**, 165123 \(2013\)](#).
- [26] P. A. Maksimov, Z. Zhu, S. R. White, and A. L. Chernyshev, Anisotropic-Exchange Magnets on a Triangular Lattice: Spin Waves, Accidental Degeneracies, and Dual Spin Liquids, [Physical Review X **9**, 21017 \(2019\)](#).
- [27] I. Rousochatzakis, U. K. Rössler, J. van den Brink, and M. Daghofer, Kitaev anisotropy induces mesoscopic \mathbb{Z}_2 vortex crystals in frustrated hexagonal antiferromagnets, [Physical Review B **93**, 104417 \(2016\)](#).
- [28] M. Becker, M. Hermanns, B. Bauer, M. Garst, and S. Trebst, Spin-orbit physics of $j = \frac{1}{2}$ Mott insulators on the triangular lattice, [Physical Review B **91**, 155135 \(2015\)](#).
- [29] M. Li, N. B. Perkins, and I. Rousochatzakis, Collective spin dynamics of \mathbb{Z}_2 vortex crystals in triangular Kitaev-Heisenberg antiferromagnets, [Physical Review Research **1**, 013002 \(2019\)](#).